Effect of Charge on the Rotation of Prolate Nitroxide Spin Probes in Room-Temperature Ionic Liquids

Meghan H. O'Brien,[†] Radha Ranganathan,[†] Dalibor Merunka,[‡] Alexander K. Stafford,[†] Steven D. Bleecker,[†] and Miroslav Peric*[†]

[†]Department of Physics and Astronomy, California State University, Northridge, Northridge, California 91330, United States

[‡]Division of Physical Chemistry, Ruđer Bošković Institute, Bijenička cesta 54, HR-10000

Zagreb, Croatia

* Corresponding author: miroslav.peric@csun.edu

Abstract

We have studied the rotational diffusion of two prolate nitroxide probes, the negatively doubly charged peroxylamine disulfonate (Frémy's salt - FS) and neutral di-*tert*-butyl nitroxide (DTBN), in a series of 1-alkyl-3-methylimidazolium tetrafluoroborate room-temperature ionic liquids (RTILs) having alkyl chain lengths from two to eight carbons using spin-label electron paramagnetic resonance (EPR) spectroscopy. Though the size and shape of the probes are reasonably similar, they behave differently due to the charge difference. The rotation of FS is anisotropic, and the rotational anisotropy increases with the alkyl chain length of the cation, while the rotation of DTBN is isotropic. The hyperfine coupling constant of DTBN decreases as a function of the alkyl chain length and is proportional to the relative permittivity of ionic liquids. On the other hand, the hyperfine coupling constant of FS increases with increasing chain length. These behaviors indicate the location of each probe in RTILs. FS is likely located in the polar region near the network of charged imidazolium ions. DTBN molecules are predominately distributed in the nonpolar domains.

Keywords: electron paramagnetic resonance; rotational diffusion; nitroxide radicals; rotational anisotropy; hyperfine coupling constant; room temperature ionic liquids

1. Introduction

During the last four decades, the research on room-temperature ionic liquids (RTILs) and their industrial applications have grown almost exponentially [1-5]. RTILs are salts consisting entirely of large organic cations and organic or inorganic anions. Since their structure and properties are governed mainly by Coulomb interaction between the cations and anions, which is not as strong as the one in inorganic salts [3, 6], they have peculiar and interesting physicochemical properties. Due to the weakened Coulomb forces, the RTILs have low melting temperatures and are liquids at room temperature. The potential number of RTILs is enormous due to the combination of different cations and ions [7]. Because of the large variety of combinations and their ionic nature, RTILs have unique and versatile properties, including negligible volatility, high ionic conductivity, high polarity, thermal stability, and low vapor pressure [8-10]. For that reason, RTILs are becoming the solvents of choice in many applications, such as organic synthesis [11, 12], catalysis [13-15], syntheses of new nano-sized sensor systems [16, 17], adsorption [18], electrochemistry [19], and analytical chemistry [19].

The structure and physical properties, such as solvation and polarity [20] of RTILs have been studied with different experimental methods, such as neutron diffraction [21], X-ray scattering [22], fluorescence [23, 24], and NMR spectroscopy [25, 26], to understand their use as reaction media. The spin-label electron paramagnetic resonance (EPR) method has also been shown to be extremely useful in studying the structure and physical properties of RTILs [27-30].

Small neutral and charged nitroxide probes have been used to investigate the structure, polarity, and solvation of RTILs [28, 31, 32]. From the EPR measurements of two nitroxide spin probes, 2,2,6,6-tetramethylpiperidine-1-oxyl (TEMPO) and 4-amino-2,2,6,6-tetramethylpiperidine-1-oxyl (TEMPAMINE), Noel et al. have concluded that the solvation properties of ILs are like those of polar organic solvents such as dimethylformamide and dimethyl sulfoxide [33]. Strehmel et al. [31] have applied the Gierer and Wirtz theory to explain the influence of microviscosity on the rotational correlation time of the neutral spin probes TEMPO and TEMPOL (4-hydroxy TEMPO) in a series of imidazolium-based ILs bearing either [BF_4] or [PF_6] at 293 K. They concluded that the activation of the viscous flow dominates in the investigated RTILs. Mladenova et al. have analyzed the hyperfine coupling constants and rotational correlation times of TEMPO, TEMPAMINE, TEMPOL, and peroxylamine disulfonate (PADS or Frémy's salt - FS) in the ionic liquids 1-ethyl-3-methylimidazolium ethylsulfate (EmimES), 1-ethyl-3-

methylimidazolium tetrafluoroborate ($EmimBF_4$), 1-butyl-3-methylimidazolium hexafluorophosphate ($BmimPF_6$), and 1-butyl-3-methylimidazolium tetrafluoroborate ($BmimBF_4$) [27]. Their Gierer and Wirtz theoretical analysis of the microviscosity of the spin probe's surroundings indicated that ILs might not be seen as individual ion pairs but instead as supramolecular aggregates. Using perdeuterated TEMPONE (pDTO), our group has investigated the nanostructural organization of a series of BF_4-based imidazolium RTILs with alkyl chain lengths from two to eight carbon atoms [34]. The rotational correlation time of pDTO in those RTILs was well described by the Stokes-Einstein-Debye law.

The stable, positively charged nitroxide 4-trimethylammonium-2,2,6,6-tetramethylpiperidine-1-oxyl iodide (Cat-1) has also been employed to gain insight into the physicochemical properties of ionic liquids [28-30, 35, 36]. Akdogan et al. [28] showed that Cat-1 likely resides in the polar region at the interface between the cations and anions, where it can interact with BF_4 and form a hydrogen bond with the acidic imidazolium protons, see Fig 6 in Ref [28]. Our group's measurements [36] of the ratio of the rotational times of pDTO and Cat-1, the rotational anisotropy, and the apparent activation energy of Cat-1 indicated the transition from a homogeneously globular structure to a spongelike structure when the alkyl chain has four carbons, which is also established by MD simulations [37, 38].

Miyake et al. [32, 39] have investigated the rotational motion of Frémy's salt in a variety of RTILs. From the constancy of FS's hyperfine coupling constant values for various RTILs, the authors concluded that the interaction between the $N\text{-}O^{\cdot}$ moiety, and the cation of RTIL was negligible. The large anisotropy of the FS rotation suggested a strong interaction of the negative sulfonyl parts of FS with the cations of RTILs. Using high-field/high-frequency EPR spectroscopy, Kattnig et al. studied the solvation and location of Frémy's salt in the ionic liquids $BmimBF_4$ and 1-hexyl-3-methylimidazolium tetrafluoroborate ($HmimBF_4$), and their water mixtures [40]. According to them, Frémy's salt is located in highly polar regions of these solvents. Since the spin Hamiltonian parameters of Frémy's salt remain the same throughout different solvents, they concluded that Frémy's salt environment is the same in different ionic liquids. They also observed that the molecular structure of Frémy's salt was distorted, showing an increased pyramidalization at the nitrogen center. They speculated that this molecular structure distortion points to FS being likely absorbed on the charged surface made of an array of imidazolium ions. Frémy's salt in

different RTILs was as well studied by Mladenova et al. [27]. Their EPR results also suggested that FS might be located away from the alkyl chains at the charge-bearing surface.

This article aims to explore how the hyperfine coupling constants and rotational times of two prolate nitroxide spin probes are affected by the length of the alkyl chain of BF_4-based imidazolium RTILs. Since one of the chosen nitroxides is the doubly charged peroxylamine disulfonate and the other is the neutral di-*tert*-butyl nitroxide (DTBN), but have similar shapes and sizes, we expect to gain insight into the effect of charge on the behavior of Frémy's salt in RTILs. In addition, as far as we know, DTBN has never been used in the study of RTILs, so this is the first study of this small, neutral, and prolate nitroxide spin probe in RTILs.

2. Materials and Methods

Sample Preparation

Frémy's salt and di-*tert*-butyl nitroxide (DTBN) were purchased from Aldrich Chemical Company. The room temperature ionic liquids 1-ethyl-3-methylimidazolium tetrafluoroborate (EmimBF4), 1-butyl-3-methylimidazolium tetrafluoroborate (BmimBF4), 1-hexyl-3-methylimidazolium tetrafluoroborate (HmimBF4), and 1-octyl-3-methylimidazolium tetrafluoroborate (OmimBF4) were obtained from Tokyo Chemical Industry Company. The structures of spin probes and BmimBF4 are shown in Scheme 1. All alcohols (methanol, 1-propanol, 1-butanol, 1-pentanol, 1-heptanol, 1-octanol, 1-nonanol, 1-decanol, 1-undecanol, 1-dodecanol) were bought from Fluka Chemika. All chemicals are used as received.

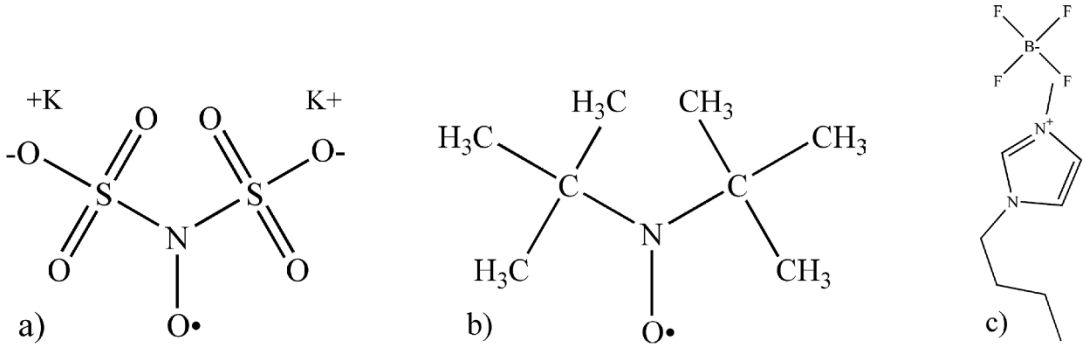

Scheme 1. Chemical structures of (a) Frémy's salt (FS), (b) di-*tert*-butyl nitroxide (DTBN), and (c) 1-butyl-3-methylimidazolium tetrafluoroborate ($BmimBF_4$).

The solutions of both chemicals were prepared by weight in each RTIL and alcohol. The concentration of FS was about 1 mM, while the concentration of DTBN was 0.2 mM. The concentration of FS was slightly larger than that of DTBN because FS decays with time. Both concentrations were low enough to avoid EPR line broadening and dispersion due to Heisenberg spin exchange and dipole-dipole interactions [41].

EPR Measurements

Before use, the RTIL solutions were kept under a vacuum for three days at room temperature. For each sample, a small amount of solution was drawn into open-ended polytetrafluoroethylene (PTFE - ID: AWG21) tubing bought from Zeus Industrial Products. The tubing was then folded, and the ends were squeezed with flat-nose pliers. The folded tubing was placed in an EPR quartz tube obtained from Wilmad, which was then inserted in the quartz Dewar insert of a Bruker N_2 temperature unit. EPR spectra were recorded by a Bruker EMXPlus EPR spectrometer equipped with the cylindrical TE_{011} ER 4119HS high-sensitivity cavity. The microwave frequency was approximately 9.3 GHz, while the microwave power was 0.5 mW. The modulation amplitude for Frémy's salt was 0.09 G, and the one for DTBN was 0.2 G. The temperature of each sample was monitored with a thermocouple setup manufactured by Omega and was maintained constant within ± 0.2 K. Measurements were mostly done between 270 K and 340 K. The lowest temperature was slightly moved depending on the viscosity of the ionic liquid, which was always less than 1000 mPa·s. Also, before the EPR measurements, we calibrated the external magnetic field according to the Bruker calibration procedure specified in the Xenon manual.

The EPR DTBN-alcohol measurements were made slightly differently. EPR measurements were made by a Bruker ESP 300E spectrometer equipped with a Bruker variable temperature unit (Model B-VT-2000) and a standard TE_{102} microwave cavity. Each sample was deoxygenated before beginning an EPR measurement until the linewidths stopped changing (approximately 60 min). Oxygen dissolves very well in alcohols [42] and, through Heisenberg spin exchange with DTBN, broadens the EPR lines, reducing the signal-to-noise ratio. For that reason, the PTFE tubing with DTBN solution was inserted into a quartz tube with a hole in the bottom to allow for

nitrogen equilibration of the sample in the EPR cavity [43]. This way, the nitrogen that controlled the temperature replaced the oxygen in the solution, reducing the DTBN EPR linewidths.

EPR Spectral Analysis

EPR spectra were fitted using the home-written computer program Lowfit. Since we have described the use of Lowfit in detail in our previous publications [44, 45], here, we will just briefly state the benefits of EPR spectral fitting [46]. Using the Dobryakov−Lebedev relation [47, 48], Lowfit extracts the peak-to-peak Lorentzian linewidth, ΔB_{pp}^{L}, from the inhomogeneously broadened observed peak-to-peak EPR linewidth, ΔB_{pp}^{O}. The Lorentzian linewidth is related to the spin-spin relaxation time, T_2, as $\Delta B_{pp}^{L} = (\frac{2}{\sqrt{3}\gamma_e})\frac{1}{T_2}$, where γ_e is the electron gyromagnetic ratio. ΔB_{pp}^{L} is used in the calculation of the rotational correlation time (see below) [49]. In addition, the resonance EPR line positions are given with a few mG precision, allowing us to have highly precise hyperfine coupling constants.

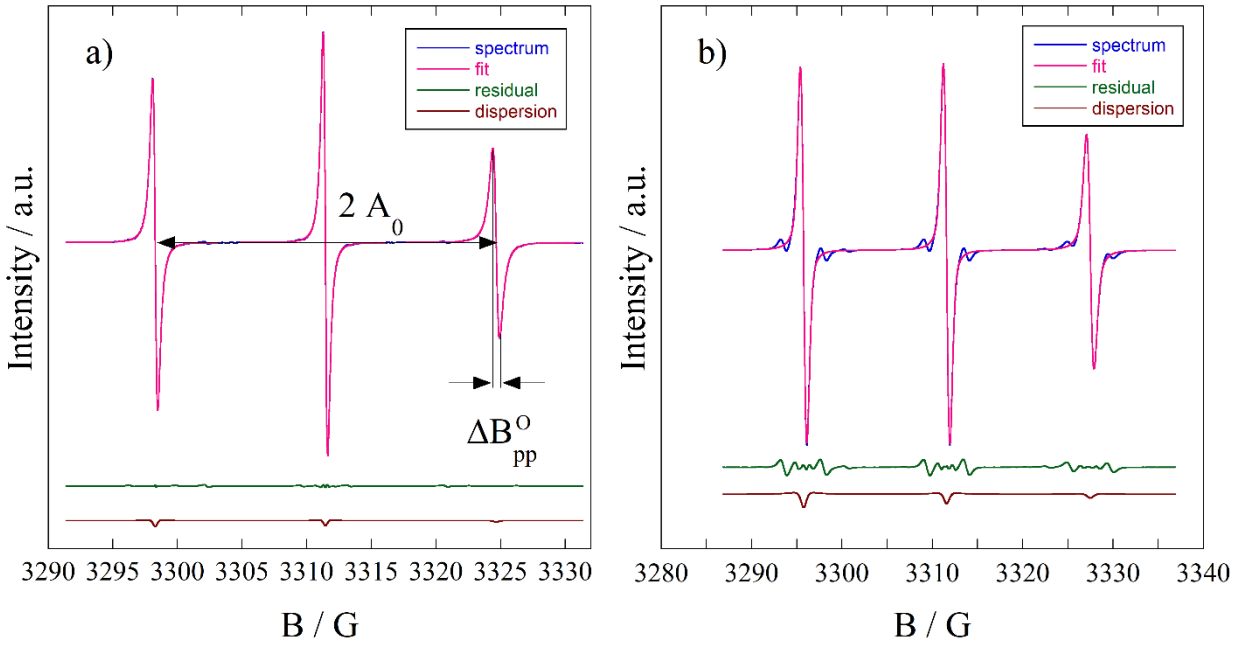

Fig. 1. The EPR spectra of (a) FS and (b) DTBN in $BmimBF_4$ at a temperature of 302 K. The upper traces show both the spectra and their fits; the fits are excellent except for the ^{13}C lines in Fig. 1b. The middle traces show the residuals, while the lower traces represent experimental dispersion. A_0 is one-half the distance between the outer lines of the ESR signal, while ΔB_{pp}^{O} is the observed peak-to-peak linewidth.

Figures 1(a) and 1(b) show the experimental EPR spectra of FS and DTBN and their fits at 302 K, respectively. The second trace in both figures is the difference between the experimental spectrum and the fit. The residual in Fig. 1(a) is flat, while the one in Fig. 1(b) has some wiggles, which come from the natural abundance of ^{13}C in DTBN, which is not included in the fit function. The bottom traces in Fig. 1(b) are due to experimental dispersion. Note that all dispersion lines have the same sign, which means that there is no Heisenberg spin exchange or dipole-dipole interactions in the solution [41, 50].

The Lorentzian EPR linewidths in the motional narrowing regime depend on the ^{14}N nuclear spin quantum number, m_I, according to:

$$\Delta B_{pp}^{L}(m_I) = A_{pp} + B_{pp} m_I + C_{pp} m_I^2 \qquad (1)$$

where m_I = +1, 0, −1 for the low-field, central, and high-field EPR lines, respectively. The linewidth coefficients A_{pp}, B_{pp}, and C_{pp} depend on the rotational correlation times and are measured in G. A_{pp} contributes equally to all three lines and originates from several homogeneous broadening mechanisms, which cannot be easily separated [51]. B_{pp} and C_{pp} can be obtained from all three Lorentzian linewidths using:

$$B_{pp} = \frac{1}{2}\left[\Delta B_{pp}^{L}(+1) - \Delta B_{pp}^{L}(-1)\right] \qquad (2a)$$

$$C_{pp} = \frac{1}{2}\left[\Delta B_{pp}^{L}(+1) + \Delta B_{pp}^{L}(-1) - 2\Delta B_{pp}^{L}(0)\right] \qquad (2b)$$

The relation between the linewidth coefficients and the rotational correlation times in the fast-motional regime can be found by time-dependent perturbation theory [49, 52]. To describe axially anisotropic rotation, we need two correlation times $\tau_{2,0}$ and $\tau_{2,2}$, which can be found from:

$$B_{pp} = \frac{8\gamma_e B_0}{45\sqrt{3}}\left[\left(1 + \frac{3}{4}\frac{1}{1+\omega_e^2\tau_{2,0}^2}\right)\Delta g \Delta A \tau_{2,0} + 3\left(1 + \frac{3}{4}\frac{1}{1+\omega_e^2\tau_{2,2}^2}\right)\delta g \delta A \tau_{2,2}\right] \qquad (3a)$$

$$C_{pp} = \frac{8\gamma_e}{45\sqrt{3}}\left[\begin{array}{l}\left(1 - \frac{3}{8}\frac{1}{1+\omega_a^2\tau_{2,0}^2} - \frac{1}{8}\frac{1}{1+\omega_e^2\tau_{2,0}^2}\right)(\Delta A)^2\tau_{2,0} \\ +3\left(1 - \frac{3}{8}\frac{1}{1+\omega_a^2\tau_{2,2}^2} - \frac{1}{8}\frac{1}{1+\omega_e^2\tau_{2,2}^2}\right)(\delta A)^2\tau_{2,2}\end{array}\right] \qquad (3b)$$

where ω_e is the electron Larmor frequency, $\omega_a = a_0/2$, where $a_0 = (A_{xx} + A_{yy} + A_{zz})/3$ is the isotropic hyperfine coupling constant, and A_{xx}, A_{yy}, and A_{zz} are the principal values of the hyperfine tensor. For rotation around the nitroxide z-axis as the principal (||) axis, the hyperfine anisotropies are:

$$\Delta A = A_{zz} - \frac{1}{2}(A_{xx} + A_{yy}) \qquad (4a)$$

$$\delta A = \frac{1}{2}(A_{xx} - A_{yy}) \qquad (4b)$$

Likewise, for the g-value anisotropies, we have:

$$\Delta g = g_{zz} - \frac{1}{2}(g_{xx} + g_{yy}) \quad (5a)$$

$$\delta g = \frac{1}{2}(g_{xx} - g_{yy}) \quad (5b)$$

where g_{xx}, g_{yy}, and g_{zz} are the principal values of the g-tensor. For the axially symmetric rotation of a nitroxide molecule about the *x*- and *y*-axes as principal axes, one needs to permute indices in Eqs. (4a) - (5b) cyclically. To find the values of $\tau_{2,0}$ and $\tau_{2,2}$, we used the function fsolve from Matlab. Next, one can find two effective rotational correlation times, one for rotation about the principal (||) axis, $\tau_{R\parallel}$, and another for rotation about a perpendicular ($\perp$) axis, $\tau_{R\perp}$, using:

$$\tau_{R\perp} = \tau_{2,0} \quad (6a)$$

$$\tau_{R\parallel} = \frac{2\tau_{2,0}\tau_{2,2}}{3\tau_{2,0} - \tau_{2,2}} \quad (6b)$$

For isotropic rotation, $\tau_{R\perp} = \tau_{R\parallel} = \tau_R$, Eqs. (3a) and (3b) become:

$$B_{pp} = \frac{8\gamma_e B_0}{45\sqrt{3}}(\Delta g \Delta A + 3\delta g \delta A)\left(1 + \frac{3}{4}\frac{1}{1+\omega_e^2\tau_R^2}\right)\tau_R \quad (7a)$$

$$C_{pp} = \frac{8\gamma_e}{45\sqrt{3}}((\Delta A)^2 + 3(\delta A)^2)\left(1 - \frac{3}{8}\frac{1}{1+\omega_a^2\tau_R^2} - \frac{1}{8}\frac{1}{1+\omega_e^2\tau_R^2}\right)\tau_R \quad (7b)$$

τ_R can be found from B_{pp} and C_{pp} by solving Eqs. (7a) and (7b). If the ratio of τ_{RB} (Eq. (7a)) and τ_{RC} (Eq. (7b)) is close to unity; the probe rotation is isotropic; otherwise, it is anisotropic. The rotational correlation time τ_R is the geometric mean of the correlation times $\tau_{R\perp}$ and $\tau_{R\parallel}$, that is $\tau_R = \sqrt{\tau_{R\parallel}\,\tau_{R\perp}}$; likewise $\tau_R = \sqrt{\tau_{RB}\,\tau_{RC}}$.

3. Results and Discussion

Rotational Anisotropy

We calculated the linewidth coefficients B_{pp} and C_{pp} for all four ionic liquids using Eqs. (2a) and (2b), respectively, from the Lorentzian linewidths. Figures 2(a) and 2(b) show C_{pp} versus $|B_{pp}|$ for FS (a) and DTBN (b) in all four ionic liquids. When $|C_{pp}/B_{pp}| \approx 1$, the nitroxide rotation is isotropic [51], the black lines in Figs. 2(a) and 2(b). On the other hand, when $C_{pp} \neq B_{pp}$, the spin probe rotation is anisotropic. Therefore, from Figs. 2(a) and 2(b), it can be observed that the rotation of FS is highly anisotropic, while the rotation of DTBN is isotropic. The same can be concluded from Fig. 1(a). Due to the anisotropic motion of FS, the low-field EPR line is broader than the central EPR line, while the high-field EPR line is even broader. Also, from the shape of

the EPR spectrum of FS, it is evident that the preferred axis of rotation for FS is the y-axis; see Fig. 7.7 from Ref. [49]. The y-axis is perpendicular to the z-axis, which lies along the nitrogen 2p atomic orbital (perpendicular to the paper plane), and the x-axis which lies along the N-O bond. In other words, the y-axis is along the line connecting the two S atoms in FS or the two central C atoms in DTBN. Next, from the slopes of the lines in Fig. 2(a) given in Table 1, one can see that the rotational anisotropy of FS increases with the alkyl chain length. The rotation of DTBN in RTILs appears to be close to isotropic, which is also indicated by similar linewidths of the low-field and central EPR lines, which also implies that $|C_{pp}/B_{pp}| \approx 1$, Table 1 and Fig. 1(b). The slight anisotropy decreases from 1.15 to 1.04 as the alkyl chain length increases, Table 1.

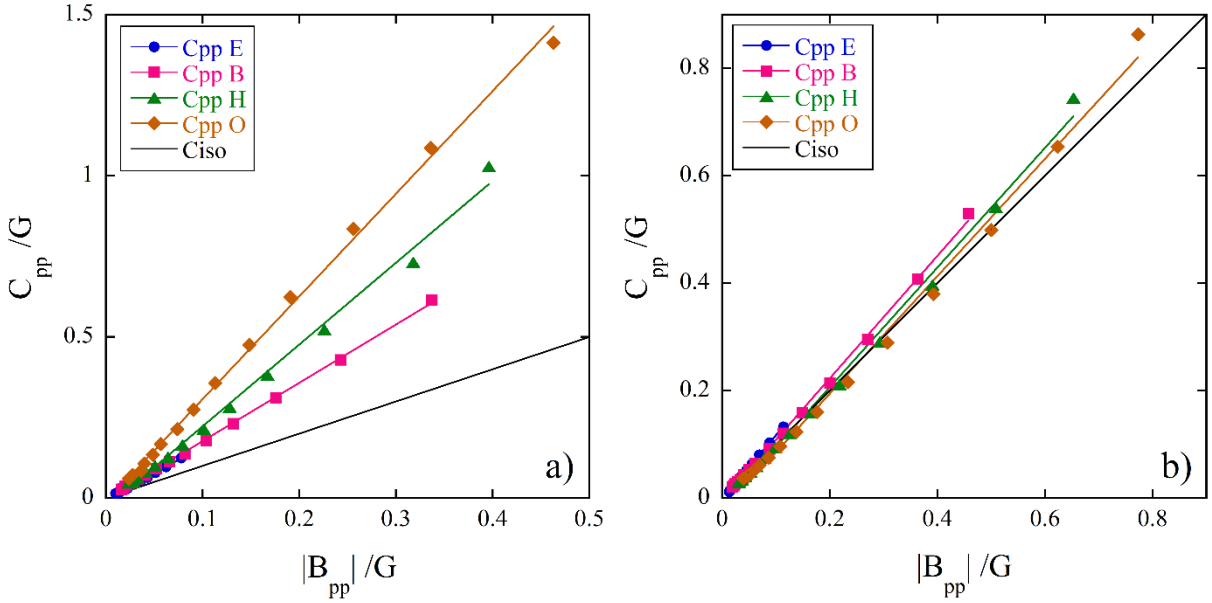

Fig. 2. Relation between C_{pp} and B_{pp} for the rotation of (a) FS and (b) DTBN in RTILs (E - $EmimBF_4$ (●); B - $BmimBF_4$ (■); H - $HmimBF_4$ (▲); and O - $OmimBF_4$ (?). The solid black lines represent isotropic rotation.

The obtained values of B_{pp} and C_{pp} were used to find the values of $\tau_{2,0}$ and $\tau_{2,2}$ or τ_R by solving Eqs. (3a) and (3b) or Eqs. (7a) and (7b), respectively. We also needed the g-value tensor and hyperfine coupling tensor principal values to solve those equations. We took rigid limit spectra of both spin probes in RTILs at low temperatures to obtain these principal values. The rigid limit EPR spectra are given in Supplemental Information, Figs. S1 and S2. Table 2 shows the principal values for g-value and hyperfine coupling tensors for FS in all four RTILs. Fig. S1 shows that all the FS EPR spectra are the same, so we assumed that the principal values are the same for all four

RTILs. The values of g_{zz} and A_{zz} were obtained from the rigid limit spectra. Goldman et al. [52] found that when <A> and <g> measured from the rigid spectrum are close to the isotropic values measured in the motional narrowing region, the principal values can be used to simulate the motionally narrowed spectrum. Therefore, g_{xx}, g_{yy}, A_{xx}, and A_{yy} values are found by fitting the fast-motional spectra of FS in RTILs using EasySpin and averaging all the values [53, 54]. Kattnig et al. [40] also found that the principal values of FS are the same in $BmimBF_4$ and $HmimBF_4$. The principal values for DTBN are presented in Table 3. The values are extracted by EasySpin rigid limit spectral fitting, Fig. S2.

Table 1. The slope coefficients of the lines in Figs.2(a) and 2(b) for FS and DTBN and their correlation coefficients, R

	$\lvert C_{pp}/B_{pp}\rvert$ (FS)	R	$\lvert C_{pp}/B_{pp}\rvert$ (DTBN)	R
$EmimBF_4$	1.53 ± 0.02	0.997	1.15 ± 0.01	0.998
$BmimBF_4$	1.78 ± 0.01	0.999	1.12 ± 0.01	0.999
$HmimBF_4$	2.40 ± 0.05	0.999	1.07 ± 0.02	0.996
$OmimBF_4$	3.14 ± 0.03	0.999	1.04 ± 0.02	0.995

Table 2. Principal g and A values for FS in all four RTILs

g_{xx}	g_{yy}	g_{zz}
2.0085 ± 0.0002	2.0053 ± 0.0002	2.0024 ± 0.0002
A_{xx} (G)	A_{yy} (G)	A_{zz} (G)
5.95 ± 0.15	4.85 ± 0.15	28.97 ± 0.31

Table 3. Principal g and A values for DTBN in all four RTILs

DTBN	g_{xx}	g_{yy}	g_{zz}	A_{xx} (G)	A_{yy} (G)	A_{zz} (G)	A_0 (G)
$EmimBF_4$	2.0087	2.0060	2.0020	7.09±0.03	5.33±0.08	35.30±0.15	15.908
$BmimBF_4$	2.0089	2.0061	2.0021	7.01±0.01	5.50±0.04	35.17±0.01	15.896
$HmimBF_4$	2.0088	2.0060	2.0020	6.98±0.01	5.61±0.02	35.03±0.01	15.877
$OmimBF_4$	2.0089	2.0060	2.0020	6.95±0.01	5.73±0.03	34.91±0.01	15.865

From $\tau_{2,0}$ and $\tau_{2,2}$, we calculated the perpendicular rotational correlation time $\tau_{R\perp}$ and parallel rotational correlation time $\tau_{R\parallel}$ for FS in RTILs using Eqs. (6a) and (6b). These values are plotted in Fig. 3(a). The data were fitted to a line without an offset, and the line slopes, which represent the rotational anisotropy $N = \tau_{R\perp}/\tau_{R\parallel}$, are presented in Table 4. Again, from Fig. 3(a) and Table 4, one can see that the rotation of FS is highly anisotropic. The rotational anisotropy increases with the alkyl chain length from 3.87 to 10. Next, τ_{RC} and τ_{RB} for DTBN in RTILs were

calculated using Eqs. (7a) and (7b) and plotted as τ_{RC} versus τ_{RB} in Fig. 3(b). The ratio τ_{RC}/τ_{RB} is also given in Table 4. Figure 3(b) and Table 4 show that the rotation of DTBN in RTILs is approximately isotropic. One can conclude that there is some slight anisotropic rotation, which decreases from $EmimBF_4$ to $OmimBF_4$. We also calculated $\tau_{R\perp}$ and $\tau_{R\parallel}$ for DTBN, but their values were noisy, and the *R* values were not very good.

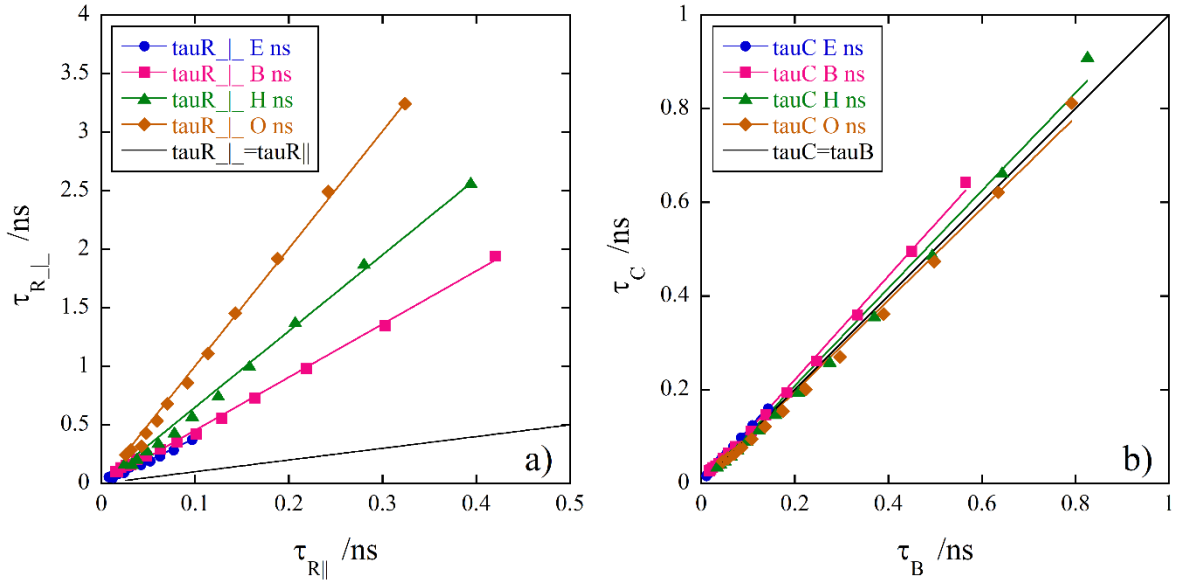

Fig. 3. (a) Correlation of $\tau_{R\perp}$ and $\tau_{R\parallel}$ for rotation of FS and (b) correlation of τ_C and τ_B for rotation of DTBN in RTILs (E - $EmimBF_4$ (●); B - $BmimBF_4$ (■); H - $HmimBF_4$ (▲); and O - $OmimBF_4$ (□). The solid black lines represent isotropic rotation.

Let us see what rotational anisotropy one can expect from geometric considerations. FS and DTBN molecules can be described as prolate axially symmetric ellipsoids, meaning the probes should have some degree of axially asymmetric rotational diffusion. From the x-ray data, the long axis of FS is $r_\parallel = r_y = 2.9$ Å, and the perpendicular axis is $r_\perp = 2.0$ Å, [55] giving the volume of FS as 48.5 Å^3. On the other side, FS van der Waals volume is 110 Å^3 [56], which is the same as the DFT calculated volume [32]. We intend to use van der Waals volumes and $r_\parallel = r_y = 3.9$ Å, and $r_\perp = 2.6$ Å from Ref. [32]. As is well known, following Perrin's approach, [57] one can calculate the effect of elliptical shape on the anisotropy of rotational diffusion of a prolate molecule [27, 49, 55, 58, 59]. A brief introduction to Perrin's approach is given in Supplemental Information. According to Eqs. (S.8), the rotational anisotropy expected from the geometric shape of FS is 1.37. The observed rotational anisotropy, which ranges from 3.87 to 10, is greater than the theoretical one,

which means that FS very likely rotates along the charged surface formed by an array of imidazolium ions as was suggested by Kattnig et al. [40]. After introducing additional experimental results, the anisotropic dependence on the alkyl chain length will be discussed below.

Table 4. Rotational anisotropy N for FS and the ratio of τ_C and τ_B for DTBN, and their correlation coefficients, R

	$N = \tau_{R\perp}/\tau_{R\parallel}$ (FS)	R	τ_{RC}/τ_{RB} (DTBN)	R
$EmimBF_4$	3.87 ± 0.09	0.986	1.15 ± 0.02	0.996
$BmimBF_4$	4.53 ± 0.04	0.999	1.11 ± 0.01	0.999
$HmimBF_4$	6.50 ± 0.07	0.998	1.04 ± 0.02	0.997
$OmimBF_4$	10.0 ± 0.1	0.998	0.98 ± 0.01	0.998

The van der Waals volume of DTBN is 164 $Å^3$ [56]. Using the electron diffraction measurements of DTBN in the vapor phase [60], we estimated $r_\parallel$ = 4.2 Å, and $r_\perp$ = 2.5 Å, which gives us $r_\parallel/r_\perp$ = 1.68. To adjust these numbers with the van der Waals volume of DTBN, we scaled the values for $r_\parallel$ and $r_\perp$, getting $r_\parallel$ = 4.8 Å, and $r_\perp$ = 2.85 Å. The rotational anisotropy expected from the geometric shape of DTBN, according to Eq. (S.8), is 1.54. As seen from Scheme 1 and the presented numbers, the shapes of FS and DTBN are very much alike. On the other hand, their observed rotational anisotropy is very different, and the reason for that is that FS is a dianion, while DTBN is neutral. Also, the two nitroxides very likely sense different parts of the solvent.

Rotational Correlation Time

The rotational correlation times of nitroxide probes can often be almost perfectly fitted to the Arrhenius equation:

$$\tau_R = \tau_{R0}\, e^{\frac{E_a}{RT}} \qquad (8)$$

where E_a is the activation energy of rotation, R is the universal gas constant, and τ_{R0} is τ_R at $T = \infty$. In the ln τ_R vs. $1/T$ plot, the activation energy represents the slope of the data, while physically, it can represent the minimum energy barrier from the surroundings, which the probe must overcome to start rotating. Therefore, E_a is sensitive to the dynamics and structure of the surrounding environment.

Figure 4 shows the temperature dependence of the perpendicular and parallel rotational correlation times for FS in RTILs as Arrhenius plots. The activation energies of $\tau_{R\perp}$ and $\tau_{R\parallel}$ are

presented in Table 5. One can notice that the activation energy of rotation for both correlation times increases with the alkyl chain length from $EmimBF_4$ to $HmimBF_4$ and then remains the same. Also, for $EmimBF_4$ and $BmimBF_4$, the activation energy of the perpendicular rotation is lower by 4 kJ/mol than the one for the parallel rotation, while for $HmimBF_4$ and $OmimBF_4$ is opposite, though the difference is less; it might not be significant. Miyake *et al.* [32] also observed the same trend for $EmimBF_4$ and $BmimBF_4$. Also, it appears that $\tau_{R\parallel}$ for $HmimBF_4$ and $OmimBF_4$ are the same, indicating that the probe's surrounding affecting the parallel rotation might be similar.

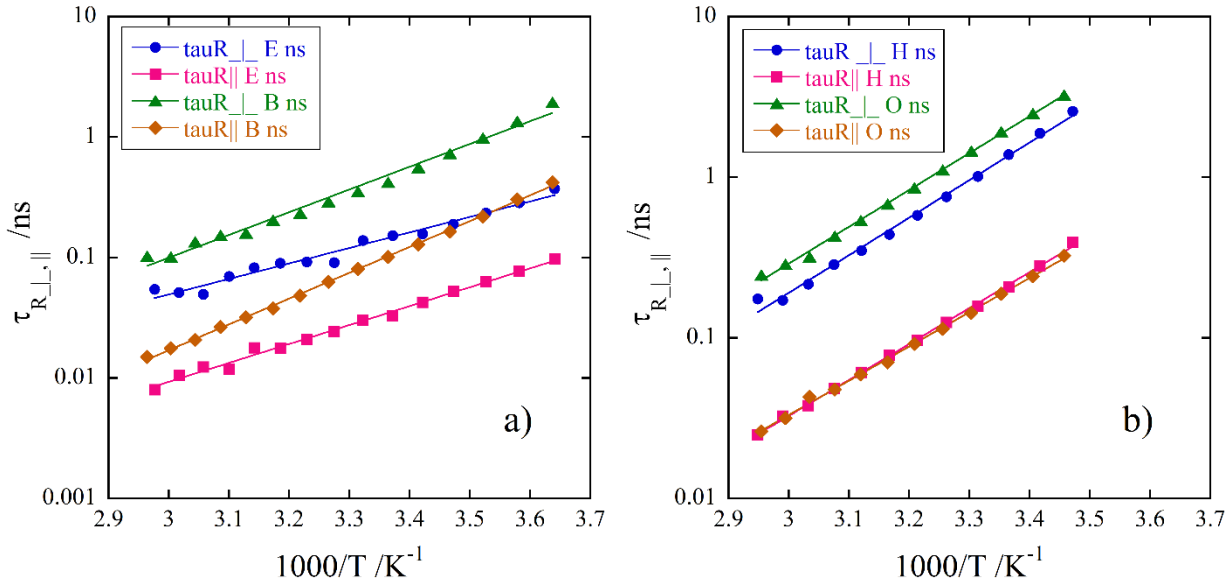

Fig. 4. Temperature dependence of the perpendicular correlation time, $\tau_{R\perp}$, and parallel correlation time, $\tau_{R\parallel}$, for rotation of FS in RTILs; (a) E – $EmimBF_4$ and B - $BmimBF_4$ and (b) H - $HmimBF_4$ and O - $OmimBF_4$. Solid lines are least-square Arrhenius fits whose slopes give activation energy for rotational diffusion.

Table 5. Activation energies of the perpendicular correlation time, $\tau_{R\perp}$, and parallel correlation time, $\tau_{R\parallel}$, for rotation of FS in RTILs and their correlation coefficients.

FS	E_a /kJ mol^{-1} ($\tau_{R\perp}$)	R	E_a /kJ mol^{-1} ($\tau_{R\parallel}$)	R
$EmimBF_4$	26.2 ± 1.1	0.990	30.4 ± 0.5	0.999
$BmimBF_4$	36.9 ± 2.0	0.990	41.0 ± 0.8	0.996
$HmimBF_4$	44.9 ± 1.0	0.999	42.9 ± 0.9	0.998
$OmimBF_4$	44.1 ± 3.3	0.999	41.2 ± 0.7	0.999

The rotational correlation times of FS and DTBN as a function of 1000/*T* are shown in Fig. 5, together with their Arrhenius fits. One can notice that the values of τ_R of FS are consistently longer than the ones for DTBN, which is expected due to the double charge of FS. Table 6 presents the activation energies for the rotation of FS and DTBN and the activation energy for the viscous flow of all four RTILs. As was explained in Ref. [34], the viscosity data are taken from the Ionic Liquids Data Base ILThermo [61, 62]. Since the activation energies for the rotation of FS and DTBN are the same as the activation energy of viscosity, the long-range dynamics likely drive their overall rotation because their different rotational anisotropies indicate that FS and DTBN probe different local environments. Mladenova *et al.* [63] also found that the activation energy of rotational diffusion of TEMPOL closely matches the activation energies of viscous flow for $EmimBF_4$, $BmimBF_4$, $OmimBF_4$, and $EmimPF_6$.

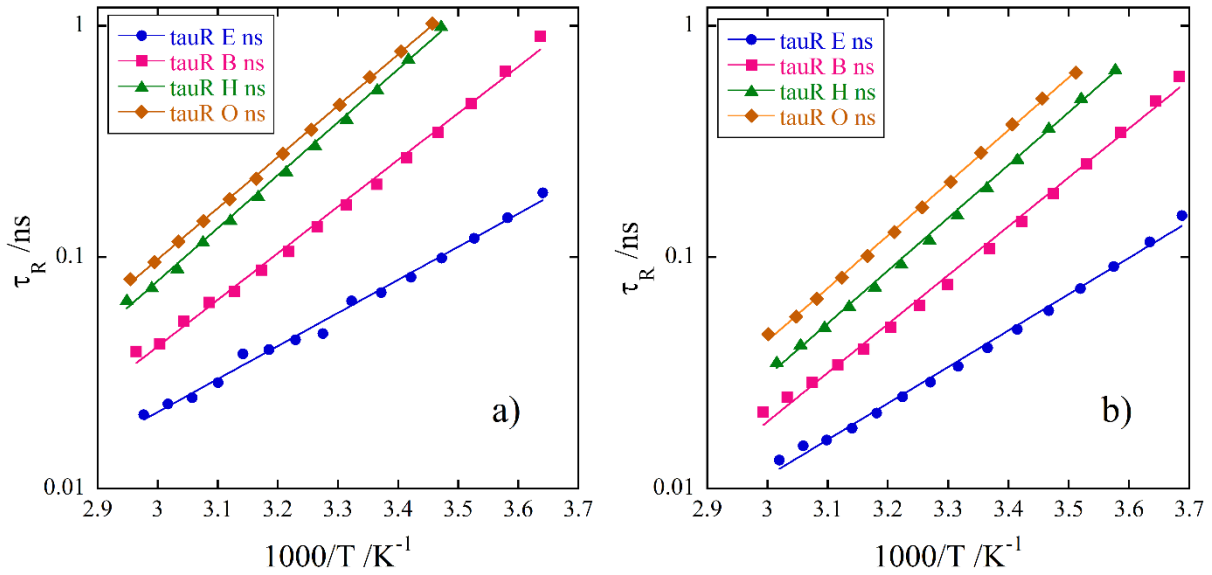

Fig. 5. Temperature dependence of the correlation time, τ_R, for rotation of FS (a) and DTBN (b) in RTILs: E - $EmimBF_4$ (●); B - $BmimBF_4$ (■); H - $HmimBF_4$ (▲); and O - $OmimBF_4$ (▯). Solid lines are least-square Arrhenius fits, giving activation energy for rotational diffusion.

Table 6. Activation energies of the rotational correlation times of FS and DTBN, and RTILs viscosity with corresponding correlation coefficients, *R*.

	E_a /kJ mol^{-1} (FS)	*R*	E_a /kJ mol^{-1} (DTBN)	*R*	E_a /kJ mol^{-1} (viscosity)	*R*
$EmimBF_4$	27.5 ± 0.8	0.997	30.3 ± 0.9	0.997	29.1 ± 0.5	0.999
$BmimBF_4$	38.9 ± 0.6	0.998	40.5 ± 1.2	0.996	38.2 ± 1.0	0.997
$HmimBF_4$	43.9 ± 1.0	0.999	44.1 ± 0.7	0.999	42.6 ± 1.2	0.998
$OmimBF_4$	42.6 ± 0.3	0.999	43.4 ± 0.5	0.999	43.4 ± 0.9	0.999

The Stokes-Einstein-Debye (SED) equation is given by:

$$\tau_R = \frac{4\pi}{3} r^3 \frac{\eta}{kT} f \qquad (9)$$

where r is the van der Waals radius of the solute, η is the shear viscosity of the surrounding solvent, k is the Boltzmann constant, and f is the slip coefficient. If $f = 1$, the rotating solute molecule is much larger than the surrounding solvent molecules, and the neighboring solvent molecules rotate together with the solute. In other words, the tangential velocity of the first layer of solvent molecules is zero, which is called the stick boundary condition. Small nitroxide molecules hardly ever satisfy $f = 1$ because nitroxides and solvent molecules' sizes are often comparable. Therefore, the value of f can be used to indicate the nature of interactions between the solute and its surroundings.

The rotational correlation times of FS and DTBN in RTILs as a function of η/T are shown in Fig. 6. Also, for comparison, the rotational correlation times expected from Eq. (9) using the van der Waals volumes of the probes, τ_{Rh}, are shown in Fig. 6. The solid lines in Fig. 6 are fitted with Eq. 9. The SED equation describes the obtained τ_R data for the covered temperature range exceptionally well. Also, it can be seen in Fig. 6 that the measured values of τ_R are much shorter than expected from hydrodynamics.

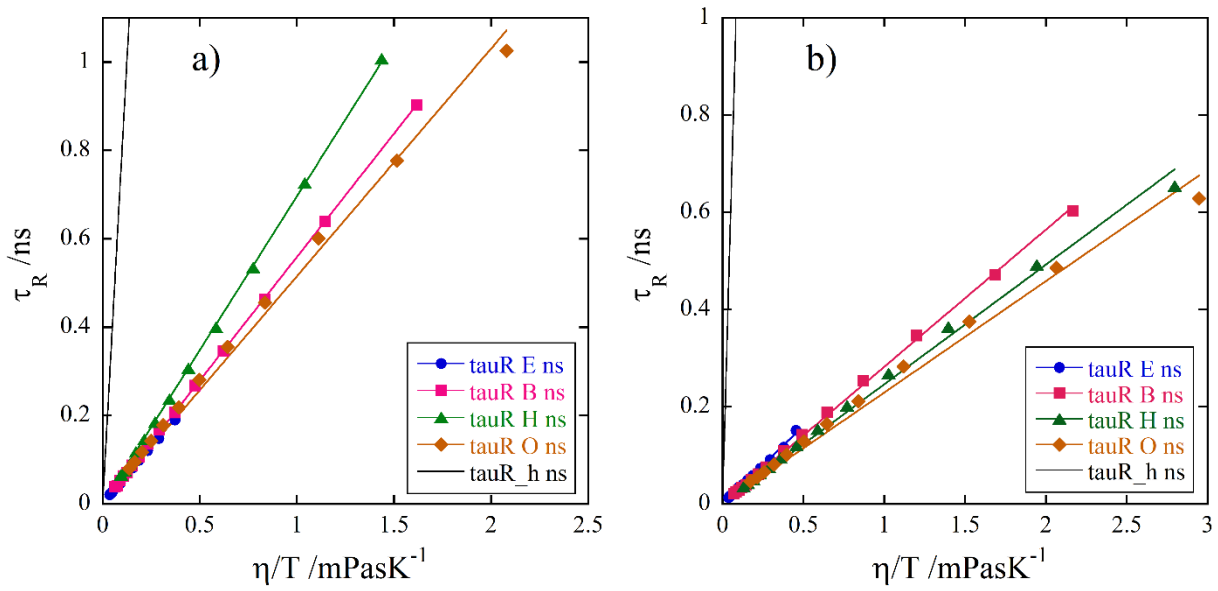

Fig. 6. Rotational correlation times, τ_R, of FS (a) and DTBN (b) versus η/T in E - $EmimBF_4$ (●), B - $BmimBF_4$ (■), H - $HmimBF_4$, (▲) and O - $OmimBF_4$ (▯). The hydrodynamic rotational correlation time τ_{Rh}, Eq. (9), is shown for comparison (solid black line). The solid lines are linear fits (without intercept).

It is common to calculate the effective hydrodynamic radius, r_{eh}, from the measured τ_R using Eq. (9), assuming $f = 1$ [55]. The effective hydrodynamic radii of FS and DTBN are presented in Table 7. We also presented the slip coefficients in parenthesis in Table 7, which is $(r_{eh}/r_{vdW})^3$. Although the van der Waals radius of DTBN (3.4 Å) is greater than the one of FS (2.98 Å), its effective hydrodynamic radius (~ 1 Å) is less than the effective hydrodynamic radius of FS (~ 1.2 Å). This means that the rotation of DTBN is less restricted than the rotation of FS in the same solvent. According to Hwang *et al.* [55], the value of r_{eh} for FS in aqueous glycerol solution is 1.16 Å, which is close to the values we obtained here, ~ 1.2 Å. Therefore, due to very low slip coefficients, less than 0.1, we can conclude that both probes rotate in cage-type vacancies and that DTBN is predominantly located in the nonpolar alkyl regions, which are less dense and where one can expect more vacancies. The electrostatic interactions between FS and imidazolium cations cause a larger effective FS radius.

Table 7. Effective hydrodynamic radii of FS and DTBN in RTILs, ratios of the effective hydrodynamic radius to the van der Waals radius, and the corresponding slip coefficients in parenthesis.

	r_{eh}, Å (FS)	r_{eh}/r_{vdW} (f)	r_{eh}, Å (DTBN)	r_{eh}/r_{vdW} (f)
$EmimBF_4$	1.21	0.41 (0.067)	1.03	0.30 (0.028)
$BmimBF_4$	1.23	0.41 (0.070)	0.98	0.29 (0.024)
$HmimBF_4$	1.28	0.43 (0.079)	0.95	0.28 (0.022)
$OmimBF_4$	1.20	0.40 (0.065)	0.94	0.28 (0.021)

Hyperfine Coupling Constant

The hyperfine coupling constant of the nitroxide free radical is sensitive to the micropolarity of its surroundings [49]. Higher surrounding micropolarity boosts the unpaired electron spin density on the nitrogen atom, which increases the hyperfine coupling constant. This behavior has been well-established for conventional solvents and many RTILs [27, 31]. Figure 7 displays the hyperfine coupling constant of FS in RTILs, water, and methanol as a function of temperature. The A_0 values for $EmimBF_4$, $BmimBF_4$, water, and methanol appear to increase linearly with temperature in the temperature range studied. However, a different, nonlinear temperature dependence can be seen in $HmimBF_4$ and $OmimBF_4$.

Based on the behavior of the hyperfine coupling constant of pDTO, Cat-1, TEMPOL, TEMPO, and TEMPAMINE, [27, 34, 36] one would expect that the value of A_0 in the fast-motional regime would decrease as the alkyl chain length increases at the same temperature. Here, we

observe the opposite behavior for FS: the value of A_0; in other words, the micropolarity sensed by FS increases. In Fig. 7, we also included the hyperfine coupling constants of FS in water and methanol for comparison. Since methanol's permittivity is less than water's, as expected, the value of A_0 in methanol is less than in water. Therefore, the most likely explanation for the opposite behavior of FS is that FS in RTILs is in the region close to the surface of charged imidazolium ions in the polar nanodomain. As the nanostructure morphology changes from homogeneously distributed polar and nonpolar domains in $EmimBF_4$ to 3-D dimensional bicontinuous spongelike nanostructure in the longer chain RTILs, as explained in Refs. [37] and [38], the continuous charged surface increases. This change, in turn, increases the electrostatic interactions between the FS dianion and the positive imidazolium surface, moving FS toward a more polar environment and increasing the value of A_0. In the case of water and methanol, FS senses a homogenous environment. In addition, since methanol is less polar, A_0 behaves as expected.

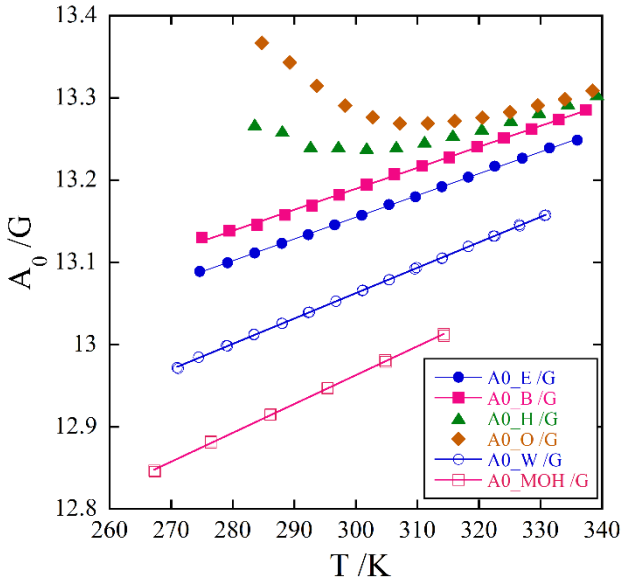

Fig. 7. Hyperfine coupling constant A_0 of FS versus T in E - $EmimBF_4$ (●), B - $BmimBF_4$ (■), H - $HmimBF_4$, (▲), O - $OmimBF_4$ (?), W - water (○), and MOH - methanol (□). The straight solid lines are linear fits.

The increase in A_0 is also supported by the decrease in ion dissociation, the number of free ions divided by the total number of ions in the ionic liquid, observed in C_nmimBF_4, where n = 2, 4, 6, and 8, Figure 10 in Ref. [64]. Increasing the number of alkyl carbons decreases the electrostatic interaction between cations and anions due to the decreased concentration of cationic

headgroups and increases the van der Waals interaction between the alkyl chains. The result of the competing interactions is the formation of nonpolar and polar nanodomains. The observed decrease in ion dissociation [64] indicates that, at the same time, the overall strength of the attraction between the ion pairs increases. Therefore, the attraction between FS and cation headgroups also increases with alkyl chain length, producing an increase in A_0.

According to Bullock *et al.* [65], the temperature dependence of A_0 depends on the angle between the C-N-C plane and the N-O· bond, which in turn depends on the minimum configuration of nitroxide. If the C-(N-O·)-C configuration is planar, then the potential energy governing out-of-plane vibrations will have one minimum, and A_0 has a positive temperature dependence. When the C-(N-O·)-C configuration is pyramidal, then the potential energy governing out-of-plane vibrations will have a symmetric double minimum. In this case, the temperature dependence of A_0 depends on the height of the barrier to inversion. If the barrier is large enough, having at least three vibrational levels, then at low temperatures, the temperature dependence of A_0 will be negative, and as the temperature continues increasing, the change in A_0 will go through zero and start increasing [65]. Conversely, when the inversion barrier is low, having less than three vibrational levels, the value of A_0 increases monotonically with temperature. Accordingly, it is not always easy to distinguish between the planar and double minimum low barrier inversion configurations.

The temperature dependence of A_0 for FS in $HmimBF_4$ and $OmimBF_4$ indicates that the C-(N-O·)-C configuration in FS is pyramidal with a symmetric double potential minimum. The inversion barrier is sufficiently high for there to exist at least three vibrational levels below the top of the barrier, with two of these levels nearly degenerate, and the barrier in $OmimBF_4$ (T_{A0min} ~ 310 K) is higher than in $HmimBF_4$ (T_{A0min} ~ 300 K). Kattnig *et al*. [40] also speculated that FS in $HmimBF_4$ experiences an increased pyramidalization at the nitrogen center. We observed a linear temperature dependence in the measured temperature range for the other two ionic liquids. However, Mladenova *et al.* [27] observed a minimum in $BmimPF_6$ (T_{A0min} ~ 265 K), which could indicate that such a minimum also exists in $BmimBF_4$ below our measured temperature range. The temperature coefficients, dA_0/dT, we obtained for the slopes in $EmimBF_4$ and BmimBF, are 2.65 ± 0.01 mG/K (R=0.99984) and 2.55 ± 0.02 mG/K (R=0.99933), respectively, which is the same (2.56 ± 0.07 mG/K) as in Ref. [27]. As mentioned, for the remaining three cases ($EmimBF_4$, water, and methanol), it is impossible to know whether the C-(N-O·)-C configuration is planar or pyramidal with a double minimum low barrier inversion. Also, the temperature coefficient for

water, which is 3.09 mG/K, is the same as the one measured by Bales *et al.* [66]. Since FS in methanol has not been measured before, we present its A_0 temperature dependence in the 167 to 314 K temperature range in Fig S3 (Supplemental Information).

The hyperfine coupling constant of DTBN in RTILs as a function of temperature is presented in Fig. 8. The value of A_0 decreases with the alkyl chain length, as expected. Another interesting feature is that A_0 is constant over most of the temperature range and starts decreasing at lower temperatures when viscosity rapidly increases.

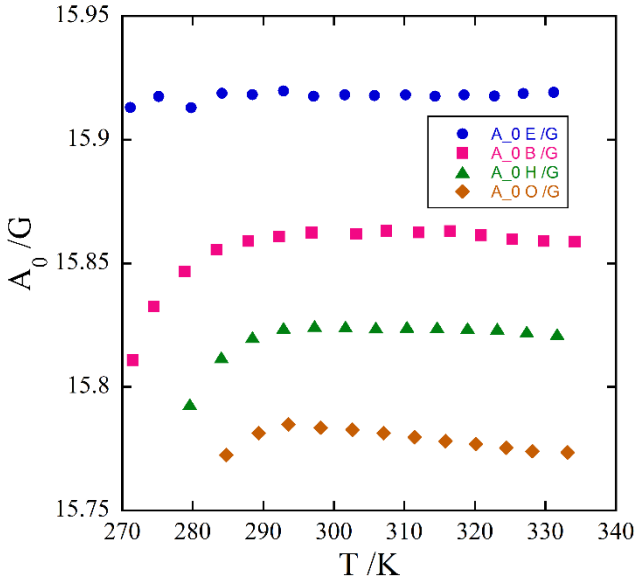

Fig. 8. Hyperfine coupling constant A_0 of DTBN versus T in E - $EmimBF_4$ (●), B - $BmimBF_4$ (■), H - $HmimBF_4$, (▲), and O - $OmimBF_4$ (□).

Mukerjee *et al.* [67] demonstrated that the hyperfine coupling constant of a nitroxide is linearly dependent on the relative permittivity of the solvent. This can be seen in Fig. 9, which shows the value of A_0 in water and a series of n-alcohols versus relative permittivity ε at room temperature. The solid line in Fig. 9 is a linear fit to the data and is described by $A_0 = (15.736 \pm 0.005) + (0.0163 \pm 0.0003)\ \varepsilon$, with $R = 0.994$. This equation can be used to estimate the relative permittivity sensed by DTBN. The relative permittivities at room temperature are 11 for $EmimBF_4$, 7.6 for $BmimBF_4$, 5.3 for $HmimBF_4$, and 3 for $OmimBF_4$. These values are close but slightly lower than the relative permittivity values measured at zero frequency using a coaxial probe technique by Bennett *et al.* [68], which are 12.9 ($EmimBF_4$), 9.7 ($BmimBF_4$), and 8.4 ($HmimBF_4$); Table 2

in Ref. [68]. The slightly lower values sensed by DTBN may indicate that DTBN spends a bit more time in the nonpolar than polar domains.

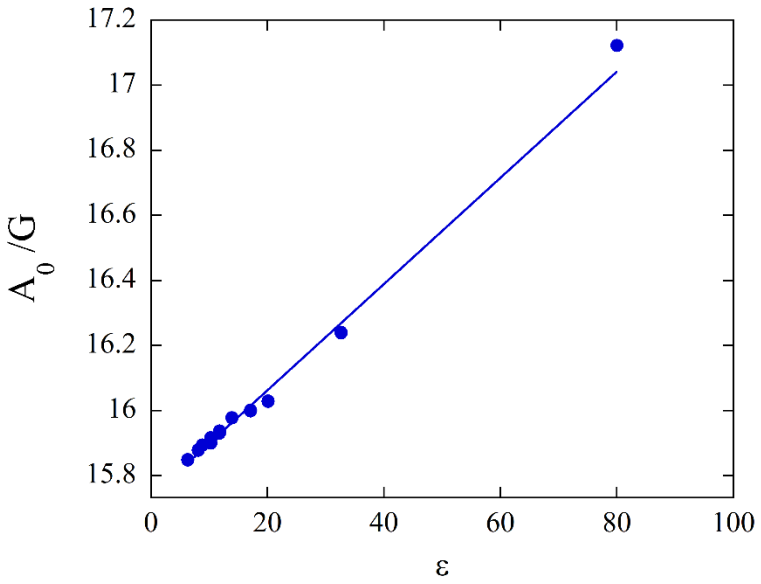

Fig. 9. Hyperfine coupling spacings A_0 of DTBN versus relative permittivity ε in water, methanol, propanol, butanol, pentanol, heptanol, octanol, nonanol, decanol, undecanol, and dodecanol (from top to bottom) at room temperature.

4. Conclusions

Although FS and DTBN are both prolate molecules with similar sizes and anisotropies, their rotational behavior in all four RTILs differs significantly. Undoubtedly, the reason for different behavior comes from their charge difference, which makes them reside in different domains of the studied RTILs.

Frémy's salt resides in the polar domain near the network of charged imidazolium ions. Two sulfonyl groups with negative charges are electrostatically attracted to the RTIL cations, so the molecule preferentially rotates about its y-axis, which connects the two negative charges. The rotation about this axis is represented by $\tau_{R\|}$. It is several times faster than the perpendicular rotation, even though, according to Perrin's theoretical arguments based on FS geometry, it should be only slightly faster (about 37%). As the cation alkyl chain increases, the rotation anisotropy N increases from 3.87 in $EmimBF_4$ to 10 in $OmimBF_4$. This increase likely happens because the charge-bearing network of the 3-D dimensional bicontinuous spongelike nanostructure becomes

better interconnected as the nonpolar regions grow. In addition, the slight increase in the hyperfine coupling constant indicates that the electrostatic attraction increases and FS moves closer to the positively charged network. The probe location change restricts the out-of-plane vibrations of the C-(N-O·)-C pyramidal configuration of FS, which, in turn, affects the height of the barrier to inversion of the pyramidal configuration so that the height of the barrier increases from ~ 265 K in $BmimPF_4$ to ~ 310 K in $OmimBF_4$.

The location and behavior of Frémy's salt in methylimidazolium BF_4 RTILs can also be explained by the decrease of ion dissociation in the same ionic liquids observed by Nordness and Brennecke [64]. According to them, in the case of weakly coordinating and lower charged density anion BF_4^-, the increased number of alkyl carbons decreases electrostatic attraction while, at the same time, increasing the overall strength of the attraction between the cationic headgroups and negatively charged anions, in our case, both BF_4^- and Frémy's salt.

Since it is neutral, DTBN moves freely throughout the RTIL volume but spends more time in the nonpolar alkyl domains. For this reason, the rotation of DTBN is nearly isotropic even though, according to Perrin's geometrical considerations, the rotational anisotropy is 1.54. The hyperfine coupling constant of DTBN decreases with increasing cation alkyl chain length. Based on the alcohol calibration curve, Fig. 9, the relative permittivities of RTILs at room temperature are close but slightly lower than the relative permittivity values measured at zero frequency using a coaxial probe technique.

The activation energies for the rotation of FS and DTBN are the same and are the same as the activation energy of viscosity. Since the local environments and the rotational anisotropy of the probes are different, but the energy required for the probe to rotate is the same as the energy required to overcome the viscous resistance from the solvent molecules, the long-range dynamics likely drive their overall rotation. The SED equation with the slip boundary conditions fits the rotational correlation times of FS and DTBN in RTILs. The slip coefficients are less than 0.1 and thus indicate that both probes rotate in cage-type vacancies. Even though the van der Waals radius of DTBN is about 13% larger than the van der Waals radius of FS, the slip coefficient for FS is about two times larger than the one for DTBN. This relationship means that the rotation of DTBN is less restricted than the rotation of FS in the same solvent, which is due to the probes' different locations, as mentioned above.

Graphical abstract

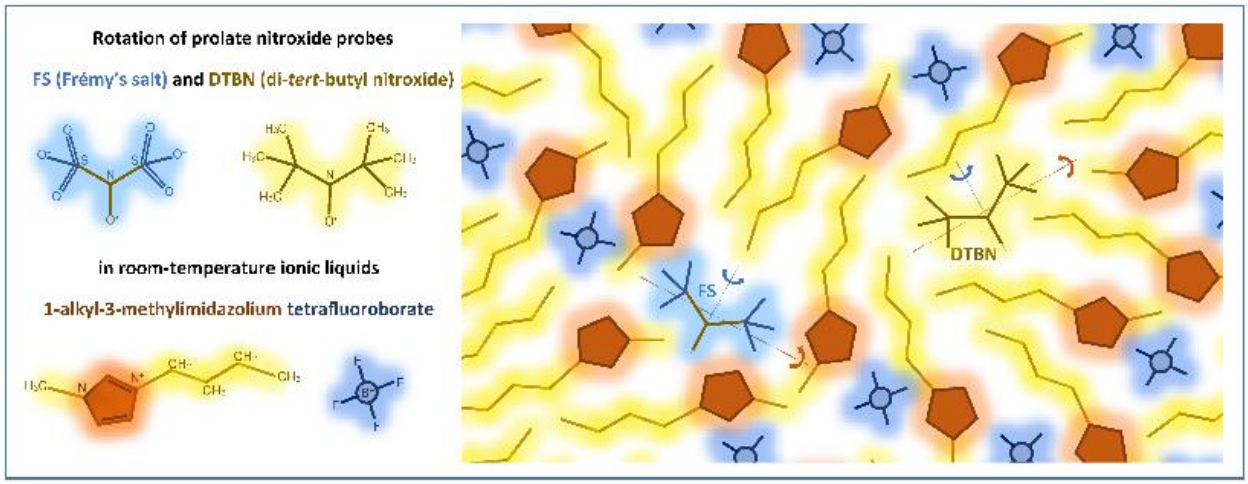

Highlights

Doubly charged peroxylamine disulfonate – Frémy's salt – resides in the polar nanodomains of room-temperature ionic liquids.

Neutral di-*tert*-butyl nitroxide – DTBN – resides in the nonpolar nanodomains of room-temperature ionic liquids.

Rotational anisotropy of Frémy's salt increases with increasing cation alkyl chain length.

The activation energy of the rotation of Frémy's salt and di-*tert*-butyl nitroxide is the same as that of the viscous flow.

Long-range collective motion governs the activation energy of Frémy's salt and di-*tert*-butyl nitroxide rotation.

Declaration of Competing Interest

The authors declare that they have no known competing financial interests or personal relationships that could have appeared to influence the work reported in this paper.

Data availability

Data will be made available on request.

Acknowledgments

M. H. O'Brien and M. Peric gratefully acknowledge support from NSF RUI (grant no. 1856746). R. Ranganathan gratefully acknowledges NIH's support through grant contracts # 1SC3GM122499-01A1 and 1SC3GM144158- 01. D. Merunka gratefully acknowledges support from the Croatian Science Foundation (Project HRZZ-IP-2022-10-9292).

References:

[1] E.W. Castner, J.F. Wishart, Spotlight on ionic liquids, J. Chem. Phys. 132 (2010) 120901.
[2] M.J. Earle, K.R. Seddon, Ionic Liquids. Green Solvents for the Future, Pure Appl. Chem. 72 (2000) 1391-1398.
[3] T. Welton, Ionic liquids: a brief history, Biophysical Reviews 10 (2018) 691-706.
[4] D.D. Patel, J.-M. Lee, Applications of Ionic Liquids, Chem. Rec. 12 (2012) 329−355.
[5] J.F. Wishart, Energy applications of ionic liquids, Energy Environ. Sci. 2 (2009) 956-961.
[6] J. Płotka-Wasylka, M. de la Guardia, V. Andruch, M. Vilková, Deep eutectic solvents vs ionic liquids: Similarities and differences, Microchemical Journal 159 (2020) 105539.
[7] N.V. Plechkova, K.R. Seddon, Applications of ionic liquids in the chemical industry, Chem. Soc. Rev. 37 (2008) 123-150.
[8] N. Ito, R. Richert, Solvation Dynamics and Electric Field Relaxation in an Imidazolium-PF6 Ionic Liquid: from Room Temperature to the Glass Transition, J. Phys. Chem. B 111 (2007) 5016-5022.
[9] J.G. Huddleston, H.D. Willauer, R.P. Swatloski, A.E. Visser, R.D. Rogers, Room Temperature Ionic Liquids as Novel Media for 'Clean' Liquid–Liquid Extraction, Chem. Commun. (1998) 1765–1766.
[10] S.N. Baker, G.A. Baker, F.V. Bright, Temperature-Dependent Microscopic Solvent Properties of 'Dry' and 'Wet' 1-Butyl-3-methylimidazolium Hexafluorophosphate: Correlation with $E_T(30)$ and Kamlet–Taft Polarity Scales, Green Chem. 4 (2002) 165-169.
[11] M. Freemantle, Ionic Liquids in Organic Synthesis, Chem. Eng. News 82 (2004) 44-49.
[12] T. Itoh, Ionic Liquids as Tool to Improve Enzymatic Organic Synthesis, Chemical Reviews 117 (2017) 10567-10607.
[13] T. Welton, Room-Temperature Ionic Liquids. Solvents for Synthesis and Catalysis, Chemical Reviews 99 (1999) 2071-2084.
[14] C.M. Gordon, New Developments in Catalysis Using Ionic Liquids, Appl. Catal. A: General 222 (2001) 101-117.
[15] P. Wasserscheid, W. Keim, Ionic Liquids - New "Solutions" for Transition Metal Catalysis, Angew.Chem. Int. Ed. 39 (2000) 3772-3789.
[16] J.F. Wishart, J. Castner, E W., The Physical Chemistry of Ionic Liquids, J. Phys. Chem. B 111 (2007) 4639-4640.
[17] R.D. Rogers, G.A. Voth, Ionic Liquids, Acc. Chem. Res. 40 (2007) 1077-1078.
[18] I.A. Lawal, M. Klink, P. Ndungu, B. Moodley, Brief bibliometric analysis of "ionic liquid" applications and its review as a substitute for common adsorbent modifier for the adsorption of organic pollutants, Environmental Research 175 (2019) 34-51.
[19] J.L. Anderson, D.W. Armstrong, G.-T. Wei, Ionic Liquids in Analytical Chemistry, Analytical Chemistry 78 (2006) 2892-2902.

[20] C. Hardacre, J.D. Holbrey, M. Nieuwenhuyzen, T.G.A. Youngs, Structure and Solvation in Ionic Liquids, Accounts of Chemical Research 40 (2007) 1146-1155.
[21] C. Hardacre, J.D. Holbrey, S.E.J. McMath, D.T. Bowron, A.K. Soper, Structure of molten 1,3-dimethylimidazolium chloride using neutron diffraction, The Journal of Chemical Physics 118 (2003) 273-278.
[22] M. Zhao, B. Wu, E.W. Castner Jr., Mixtures of octanol and an ionic liquid: Structure and transport, J. Chem. Phys. 153 (2020) 214501.
[23] C. Lawler, M.D. Fayer, The Influence of Lithium Cations on Dynamics and Structure of Room Temperature Ionic Liquids, J. Phys. Chem. B 117 (2013) 9768-9774.
[24] V. Gangamallaiah, G.B. Dutt, Effect of Alkyl Chain Length on the Rotational Diffusion of Nonpolar and Ionic Solutes in 1-Alkyl-3-Methylimidazolium-bis(trifluoromethylsulfonyl)imides, J. Phys. Chem. B 117 (2013) 12261-12267.
[25] A. Kaintz, G. Baker, A. Benesi, M. Maroncelli, Solute Diffusion in Ionic Liquids, NMR Measurements and Comparisons to Conventional Solvents, J. Phys. Chem. B 117 (2013) 11697-11708.
[26] C.A. Rumble, A. Kaintz, S.K. Yadav, B. Conway, J.C. Araque, G.A. Baker, C. Margulis, M. Maroncelli, Rotational Dynamics in Ionic Liquids from NMR Relaxation Experiments and Simulations: Benzene and 1-Ethyl-3-Methylimidazolium, J. Phys. Chem. B 120 (2016) 9450-9467.
[27] B.Y. Mladenova, D.R. Kattnig, G.n. Grampp, Room-Temperature Ionic Liquids Discerned Via Nitroxyl Spin Probe Dynamics, J. Phys. Chem. B 115 (2011) 8183-8198.
[28] Y. Akdogan, J. Heller, H. Zimmermann, D. Hinderberger, The Solvation of Nitroxide Radicals in Ionic Liquids Studied by High-Field EPR Spectroscopy, Phys. Chem. Chem. Phys. 12 (2010) 7874-7882.
[29] D.R. Kattnig, Y. Akdogan, I. Lieberwirth, D. Hinderberger, Spin Probing of Supramolecular Structures in 1-Butyl-3-methyl-imidazolium Tetrafluoroborate/Water Mixtures, Mol. Phys. 111 (2013) 2723-2737.
[30] V. Strehmel, S. Berdzinski, H. Rexhausen, Interactions between ionic liquids and radicals, J. Mol. Liq. 192 (2014) 153-170.
[31] V. Strehmel, A. Laschewsky, R. Stoesser, A. Zehl, W. Herrmann, Mobility of Spin Probes in Ionic Liquids, J. Phys. Org. Chem. 19 (2006) 318-325.
[32] Y. Miyake, N. Akai, A. Kawai, K. Shibuya, Hydrodynamic interpretation on the rotational diffusion of peroxylamine disulfonate solute dissolved in room temperature ionic liquids as studied by electron paramagnetic resonance spectroscopy, J. Phys. Chem. A 115 (2011) 6347-6356.
[33] M.A.M. Noel, R.D. Allendoerfer, R.A. Osteryoung, Solvation in Ionic Liquids: An EPR study, J. Phys. Chem. A 96 (1992) 2391-2394.
[34] D. Merunka, M. Peric, M. Peric, Study of Nanostructural Organization of Ionic Liquids by Electron Paramagnetic Resonance Spectroscopy, J. Phys. Chem. B 119 (2015) 3185-3193.
[35] R. Stoesser, W. Herrmann, A. Zehl, V. Strehmel, A. Laschewsky, ESR Spin Probes in Ionic Liquids, ChemPhysChem. 7 (2006) 1106-1111.
[36] J. Slade, D. Merunka, E. Huerta, M. Peric, Rotation of a Charged Spin Probe in Room-Temperature Ionic Liquids, J. Phys. Chem. B 125 (27) (2021) 7435-7446.
[37] Canongia Lopes, José N. A., A.A.H. Pádua, Nanostructural Organization in Ionic Liquids, J. Phys. Chem. B 110 (2006) 3330-3335.

[38] R. Hayes, G.G. Warr, R. Atkin, Structure and Nanostructure in Ionic Liquids, Chemical Reviews 115 (2015) 6357-6426.
[39] Y. Miyake, A. Kawai, Solvation and Rotational Diffusion of Solutes in Room Temperature Ionic Liquids as Studied by EPR Spectroscopy with Nitroxide Spin Probing Method, Applied Magnetic Resonance 49 (2018) 825-835.
[40] D.R. Kattnig, Y. Akdogan, C. Bauer, D. Hinderberger, High-Field EPR Spectroscopic Characterization of Spin Probes in Aqueous Ionic Liquid Mixtures, Zeitschrift für Physikalische Chemie 226 (2012) 1363-1378.
[41] M. Peric, B.L. Bales, M. Peric, EPR Line Shifts and Line Shape Changes Due to Heisenberg Spin Exchange and Dipole-Dipole Interactions of Nitroxide Free Radicals in Liquids: 8. Further Experimental and Theoretical Efforts to Separate the Effects of the Two Interactions J. Phys. Chem. A 116 (2012) 2855-2866.
[42] I.B. Golovanov, S.M. Zhenodarova, Quantitative Structure-Property Relationship: XXIII. Solubility of Oxygen in Organic Solvents, Russian Journal of General Chemistry 75 (2005) 1795-1797.
[43] M. Peric, M. Alves, B.L. Bales, Precision Parameters from Spin-Probe Studies of Membranes Using a Partitioning Technique. Application to Two Model Membrane Vesicles., Biochim. Biophys. Acta 1669 (2005) 116-124.
[44] B.L. Bales, M. Peric, EPR Line Shifts, and Line Shape Changes Due to Spin Exchange of Nitroxide Free Radicals in Liquids 2. Extension to High Spin Exchange Frequencies and Inhomogeneously Broadened Spectra, J. Phys. Chem. A 106 (2002) 4846-4854.
[45] B.L. Bales, M. Peric, I. Dragutan, Electron Paramagnetic Resonance Line Shifts and Line Shape Changes Due to Spin Exchange between Nitroxide Free Radicals In Liquids. 3. Extension to Five Hyperfine Lines, Additional Line Shifts Due to Re-encounters, J. Phys. Chem. A 107 (2003) 9086-9098.
[46] H.J. Halpern, M. Peric, C. Yu, B.L. Bales, Rapid Quantitation of Parameters from Inhomogeneously Broadened EPR Spectra, J. Magn. Reson. A 103 (1993) 13-22.
[47] B.L. Bales, in: J.L. Berliner, J. Reuben (Eds.), Spin Labeling: Theory and Applications, Plenum, New York, 1989, p. 77-130.
[48] S.N. Dobryakov, Y.S. Lebedev, Analysis of Spectral Lines whose Profile is Described by a Composition of Gaussian and Lorentz Profiles, Sov. Phys. 13 (1969) 873-875.
[49] D. Marsh, Spin-Label Electron Paramagnetic Resonance Spectroscopy. CRC Press, Boca Raton, 2020.
[50] B.L. Bales, M. Peric, EPR Line Shifts and Line Shape Changes Due to Spin Exchange of Nitroxide Free Radicals in Liquids, J. Phys. Chem. B. 101 (1997) 8707-8716.
[51] D. Marsh, in: L.J. Berliner, J. Reuben (Eds.), Spin Labeling Theory and Applications, Plenum, New York, 1989, p. 255-303.
[52] S.A. Goldman, G.V. Bruno, C.F. Polnaszek, J.H. Freed, An ESR Study of Anisotropic Rotational Reorientation and Slow Tumbling in Liquid and Frozen Media, J. Chem. Phys. 56 (1972) 716-735.
[53] S. Stoll, A. Schweiger, EasySpin, a Comprehensive Software Package for Spectral Simulation and Analysis in EPR, J. Magn. Reson. 178 (2006) 42-55.
[54] S. Stoll, A. Schweiger, EasySpin: Simulating cw ESR Spectra, Biol. Magn. Reson. 27 (2007) 299-321.
[55] J.S. Hwang, P.R. Mason, L.-P. Hwang, J.H. Freed, Electron Spin Resonance Studies of Anisotropic Rotational Reorientation and Slow Tunbling in Liquid and Frozen Media. III.

Perdeuterated 2,2,6,6-Tetramethyl-4-Piperidone N-Oxide and An Analysis of Fluctuating Torques, J. Phys. Chem. 79 (1975) 489--511.
[56] Y.H. Zhao, M.H. Abraham, A.M. Zissimos, Fast Calculation of van der Waals Volume as a Sum of Atomic and Bond Contributions and Its Application to Drug Compounds, J. Org. Chem. 68 (2003) 7368-7373.
[57] F. Perrin, Mouvement Brownien D'un Ellipsoide(II). Rotation Libre et Depolarisation des Flourescences. Translation et Diffusion de Molecules Ellipsidales, J. Phys. Radium 7 (1936) 1-11.
[58] S.H. Koenig, Brownian motion of an ellipsoid. A correction to Perrin's results, Biopolymers 14 (1975) 2421-2423.
[59] G.R. Fleming, J.M. Morris, G.W. Robinson, Direct observation of rotational diffusion by picosecond spectroscopy, Chemical Physics 17 (1976) 91-100.
[60] B. Andersen, P. Andersen, An Electron Diffraction Investigation of the Molecular Structure of Di-t-butylnitroxide Free Radical in the Vapour Phase, Acta Chemica Scandinavica 20 (1966) 2728-2736.
[61] D. Qian, K. Andrei, M. Chris, C. Robert, W. Jason, D. Vladimir, M. Joe, M. Kenneth, F. Michael, Ionic Liquids Database (ILThermo), 2006.
[62] Q. Dong, C.D. Muzny, A. Kazakov, V. Diky, J.W. Magee, J.A. Widegren, R.D. Chirico, K.N. Marsh, M. Frenkel, ILThermo: A Free-Access Web Database for Thermodynamic Properties of Ionic Liquids, Journal of Chemical & Engineering Data 52 (2007) 1151-1159.
[63] B.Y. Mladenova, N.A. Chumakova, V.I. Pergushov, A.I. Kokorin, G. Grampp, D.R. Kattnig, Rotational and Translational Diffusion of Spin Probes in Room-Temperature Ionic Liquids, J. Phys. Chem. B 116 (2012) 12295-12305.
[64] O. Nordness, J.F. Brennecke, Ion Dissociation in Ionic Liquids and Ionic Liquid Solutions, Chemical Reviews 120 (2020) 12873-12902.
[65] A.T. Bullock, C.B.J. Howard, Temperature-Dependent Hyperfine Coupling Constants in Electron Spin Resonance. Part 6. — Planar and Non-Planar Nitroxide Radicals J. Chem. Soc., Faraday Trans. 1 76 (1980) 1296–1300.
[66] B.L. Bales, E. Wajnberg, O.R. Nascimento, Temperature-Dependent Hyperfine Coupling Constant of the Dianion Radical of Fremy's Salt, a Convenient Internal Thermometer for EPR Spectroscopy, Journal of Magnetic Resonance, Series A 118 (1996) 227-233.
[67] P. Mukerjee, C. Ramachandran, R.A. Pyter, Solvent Effects on the Visible Spectra of Nitroxides and Relation to Nitrogen Hyperfine Splitting Constants. Nonempirical Polarity for Aprotic and Hydroxilic Solvents, J. Phys. Chem. 86 (1982) 3189-3197.
[68] E.L. Bennett, C. Song, Y. Huang, J. Xiao, Measured relative complex permittivities for multiple series of ionic liquids, Journal of Molecular Liquids 294 (2019) 111571.

Effect of Charge on the Rotation of Prolate Nitroxide Spin Probes in Room-Temperature Ionic Liquids

Supplemental Information

Meghan H. O'Brien,[†] Radha Ranganathan,[†] Dalibor Merunka,[‡] Alexander K. Stafford,[†] Steven D. Bleecker,[†] and Miroslav Peric*[†]

[†]Department of Physics and Astronomy, California State University, Northridge, Northridge, California 91330, United States

[‡]Division of Physical Chemistry, Ruđer Bošković Institute, Bijenička cesta 54, HR-10000

Zagreb, Croatia

1. Rigid Limit Spectra of Frémy's Salt in RTILs

Fig. S1 represents the rigid limit spectra of Frémy's Salt (FS) in EmimBF4, BmimBF4, HmimBF4, and OmimBF4 taken at 110 K as a function of g-value. It appears that all four spectra are indistinguishable. The principal values of hyperfine coupling and g-value tensors are given in Table 2.

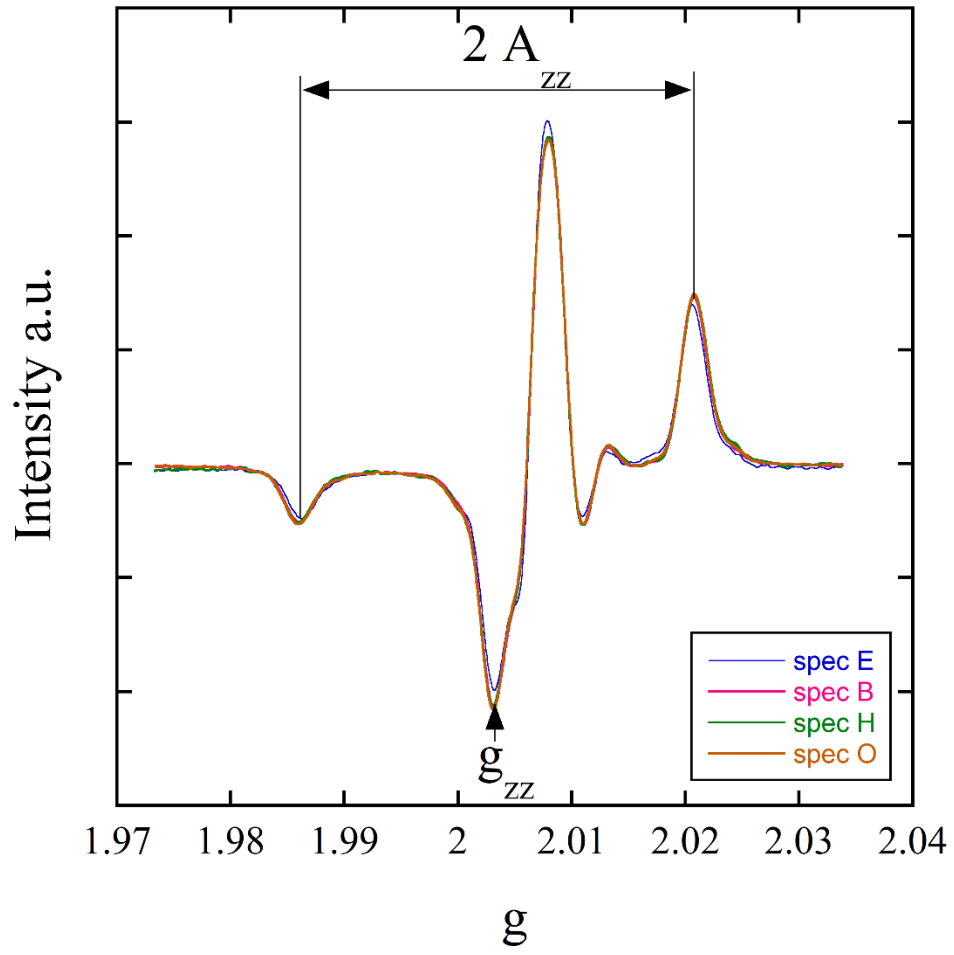

Fig. S1. The rigid limit spectra of FS in $EmimBF_4$ (blue), $BmimBF_4$ (pink), $HmimBF_4$ (green), and $OmimBF_4$ (brown) at 110 K as a function of g-value. The principal values A_{zz} and g_{zz} that can be measured from the spectrum are indicated.

2. Rigid Limit Spectrum of DTBN in $OmimBF_4$

Fig. S2 shows the EasySpin fit of neutral di-tert-butyl nitroxide (DTBN) in $OmimBF_4$. The overlapping of the spectrum and the fit, and the residual with minimal wiggles, indicate a reasonably good fit. The principal values of hyperfine coupling and g-value tensors are given in Table 3.

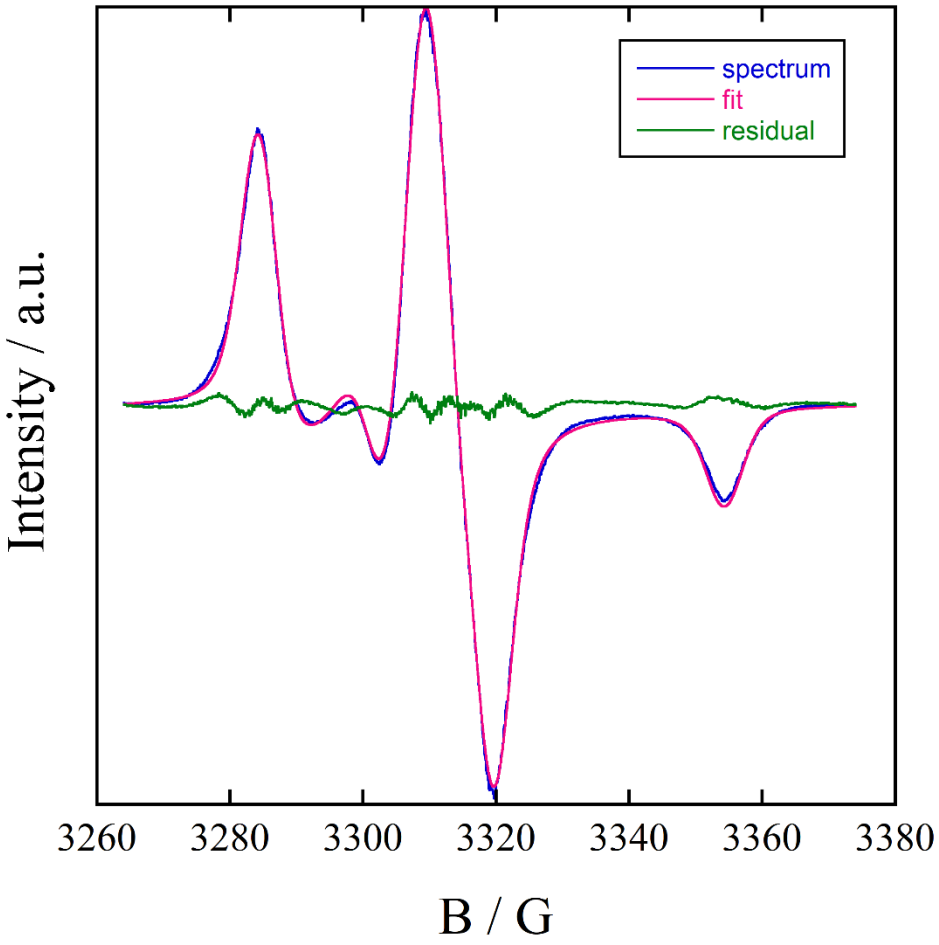

Fig. S2. The rigid limit spectrum of DTBN in $OmimBF_4$ at 110 K as a function of B. The spectrum (blue) was fit by EasySpin (pink) [1, 2]. The residual is shown in green.

3. Lowfit and EasySpin Fitting

EasySpin is a powerful software package designed to simulate, fit, and analyze Electron Paramagnetic Resonance (EPR) spectra [1, 2]. Lowfit is our homemade lineshape, which can give us very precise lineshape parameters such as line positions, linewidts, and heights when lines are Lorentzians, Gaussians, or Voigts [3, 4]. We try to validate our Lowfit approach with the EasySpin approach[5] whenever possible. Here, we have made the same. Figure S3 shows the fits of the experimental spectrum of FS in $OmimBF_4$ at 289 K fitted by both EasySpin and Lowfit. Both fits are excellent, though the EasySpin residual is somewhat worse. We do not know why that is so, but one reason might be that EasySpin does not account for experimental dispersion, which is usually less than 1 % of EPR absorption. Therefore, the two approaches should not be much different in the region where Lowfit can be used.

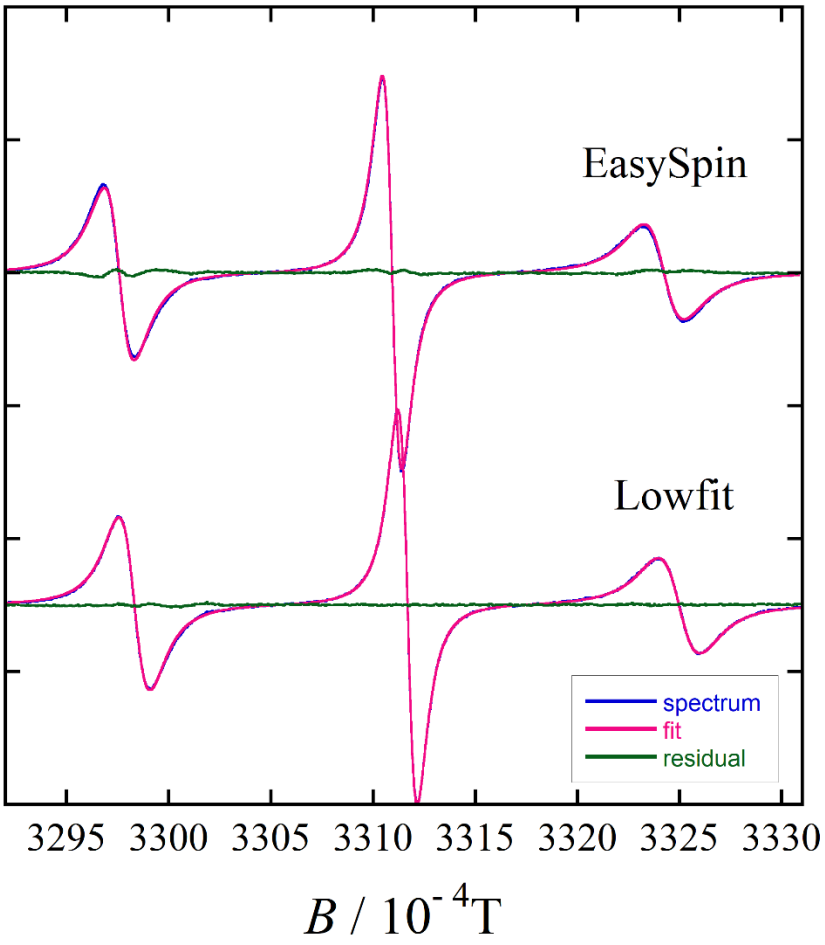

Fig. S3 The EPR spectrum of FS in $OmimBF_4$ at a temperature of 289 K fitted by EasySpin (upper traces) and Lowfit (lower traces). The experimental spectra are blue, the fits are red and the residuals are green.

In EasySpin, we varied 10 parameters: g_{xx}, g_{yy}, g_{zz}, A_{xx}, A_{yy}, A_{zz}, ΔB_{pp}^{L}, τ_{Rxx}, τ_{Ryy}, and τ_{Rzz}. We used the latest version (Version 6.0.0dev-54) with the MATLAB minimization function

lsqnonlin. Lowfit has more input parameters, but they are related to the EPR lines; that is, we have for each line its position B, observed linewidth ΔB_{pp}^{O}, absorption peak-to-peak height V_{pp}, dispersion height V_{dis}, and shape factor η, which is used to find the Lorentzian and Gaussian linewidths as described before in Refs [3, 6]. Lowfit has 3 times 5 parameters, for which the initial guesses can be found easily from the spectrum. The results of EasySpin and Lowfit fittings are shown in Fig S4. Since FS undergoes axially asymmetric rotational diffusion, we obtained τ_{Rxx}, τ_{Ryy}, and τ_{Rzz} by EasySpin. We found that τ_{Rxx} and τ_{Rzz} are very close and used their average $(\tau_{Rxx} + \tau_{Rzz})/2$ to compare to $\tau_{R\perp}$, while τ_{Ryy} is compared to $\tau_{R||}$. The agreement between the two approaches appears very good. At several temperatures, we ran EasySpin several times and found that it is slightly dependent on initial guesses. Also, the EasySpin fitting runs were much longer than the Lowfit runs due to the complexity of the fitting function. Therefore, we think that we validated our approach for current work. One should note that we also need EasySpin for the principal g and A tensor values to calculate the perpendicular and parallel correlation times using the Lorentzian linewidths extracted by Lowfit.

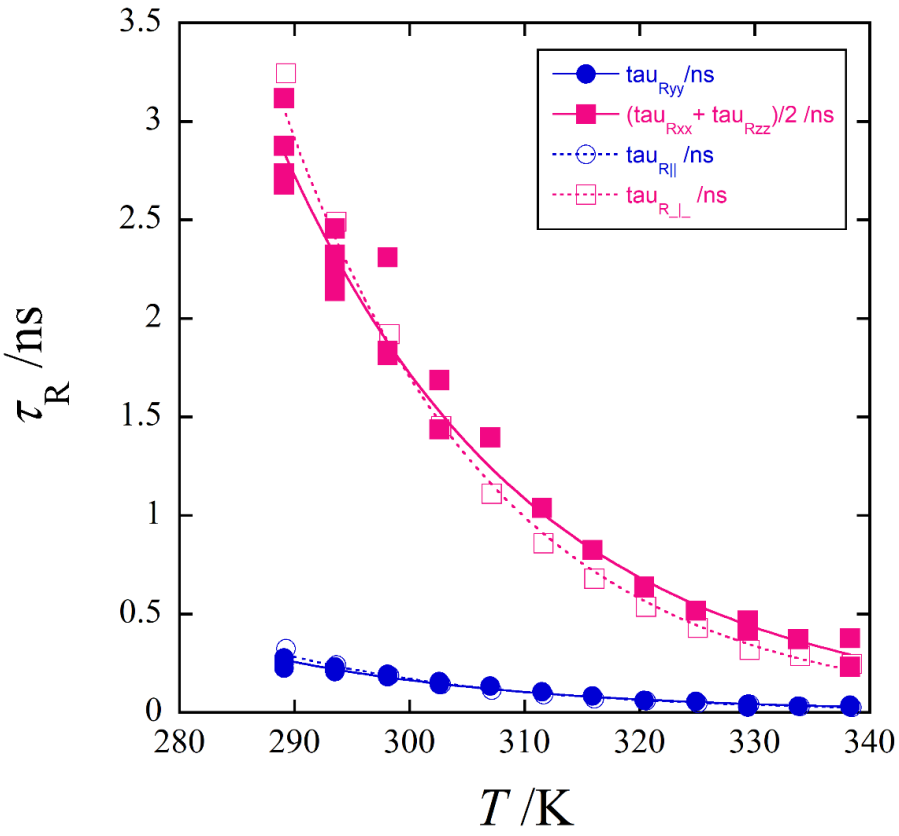

Fig. S4. The rotational correlation times τ_{Ryy} (●) and $(\tau_{Rxx} + \tau_{Rzz})/2$ (■) obtained by EasySpin, and the rotational correlation times $\tau_{R||}$ (○) and $\tau_{R\perp}$ (□) obtained by Lowfit.

In Fig. S5, we added two extra low-temperature points for the $HmimBF_4$ and $OmimBF_4$ data. Those points show that the value of A_0 starts decreasing at very high viscosities, as expected. The current data suggests that the intermediate region in the case of $HmimBF_4$ and $OmimBF_4$ likely starts below 280 K.

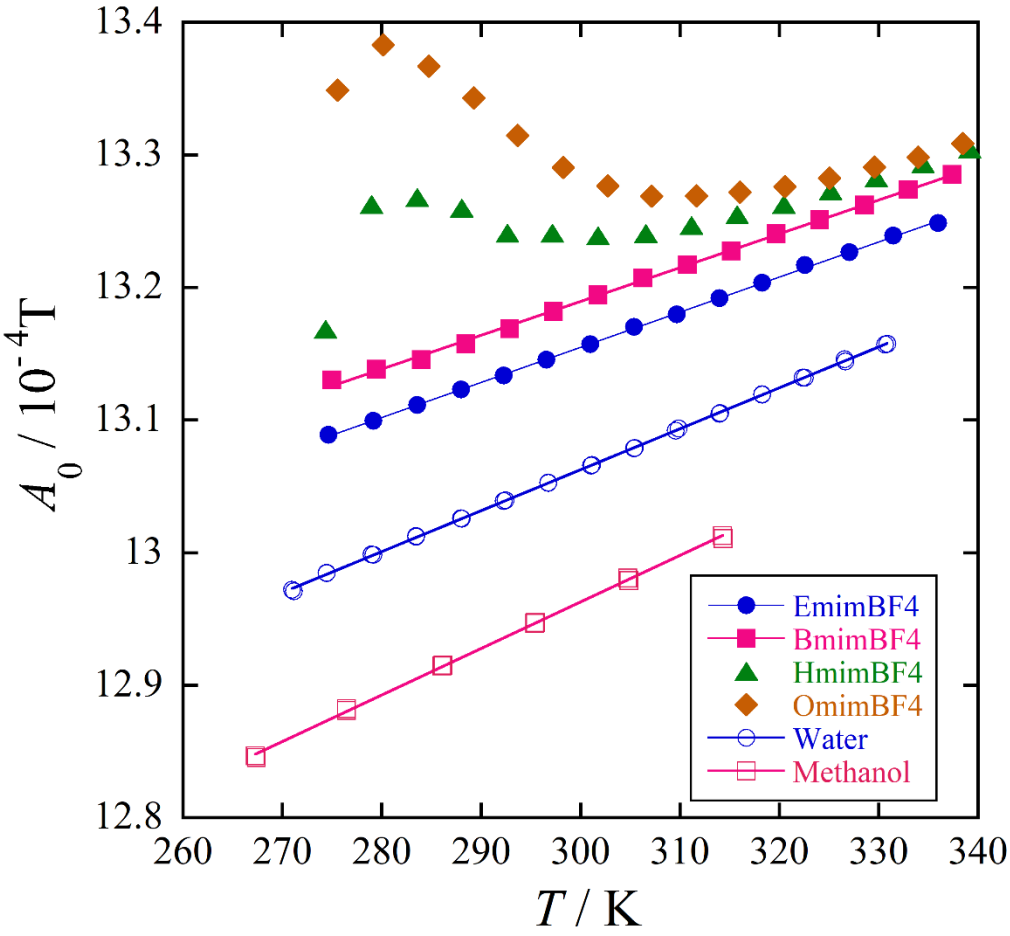

Fig. S5. Hyperfine coupling constant A_0 of FS versus T in $EmimBF_4$ (●), $BmimBF_4$ (■), $HmimBF_4$, (▲), $OmimBF_4$ (◆), water (○), and methanol (□). The straight solid lines are linear fits. This figure is the same as Fig. 8 except for two extra points added to $HmimBF_4$ and $OmimBF_4$ data at low temperatures.

4. Rotational Anisotropy

The rotational correlation times of prolate molecule about the principal symmetry axis, $\tau_{R\|}$, and perpendicular to it, $\tau_{R\perp}$, are related to the rotational diffusion coefficients $D_{R\|}$ and $D_{R\perp}$, respectively [7]:

$$\tau_{R\|} = 1/(6\, D_{R\|}) \qquad \text{(S.1)}$$

and

$$\tau_{R\perp} = 1/(6\, D_{R\perp}), \qquad \text{(S.2)}$$

where the diffusion coefficients are related to the friction coefficients through the rotational analog of the Einstein relation by[8]

$$D_R = k_B T/f_R. \qquad \text{(S.3)}$$

For a spherical particle of radius a, the frictional coefficient is

$$f_R^0 = 6\eta V_S = 8\pi\eta a^3 \qquad \text{(S.4)}$$

where V_S is the volume of the spherical particle.

For a prolate particle, the frictional coefficients have two values, $f_{R||}$ and $f_{R\perp}$, which are related to rotation around and perpendicular to the principal axis of symmetry. Perrin [9] derived the frictional coefficients for a prolate particle with semi-axes $a > b = c$ in an isotropic medium. The friction coefficient about the a (||) semi-axis is

$$f_{R||} = f_R^0 \frac{2}{3}\frac{1-\rho^2}{1-S\rho^2} \qquad \text{(S.5)}$$

and, about the b ($\perp$) semi-axis is

$$f_{R\perp} = f_R^0 \frac{2}{3\rho^2}\frac{1-\rho^4}{S(2-\rho^2)-1}, \qquad \text{(S.6)}$$

where for a rodlike particle $\rho = b/a = r_\perp / r_{||} < 1$, S is defined as

$$S = \frac{1}{\sqrt{1-\varrho^2}} \ln\left(\frac{1+\sqrt{1-\varrho^2}}{\varrho}\right). \qquad \text{(S.7)}$$

Finally, rotational anisotropy is

$$N = \frac{\tau_{R\perp}}{\tau_{R||}} = \frac{D_{R||}}{D_{R\perp}} = \frac{f_{R\perp}}{f_{R||}}. \qquad \text{(S.8)}$$

5. **Hyperfine Coupling Constant of Frémy's Salt in Methanol**

Fig. S5 shows the hyperfine coupling constant of Fremy's salt vs temperature in methanol. The measurements were fitted to a linear function:

$$A(T) = A_0(T) + \frac{\partial A(T)}{\partial T} T \qquad \text{(S.9)}$$

The measurement yields

$$A(T) = (11.881 \pm 0.002)\times 10^{-4} + (0.003609 \pm 0.00001)10^{-4} T \qquad \text{(S.10)}$$

The correlation coefficient R is 0.99989.

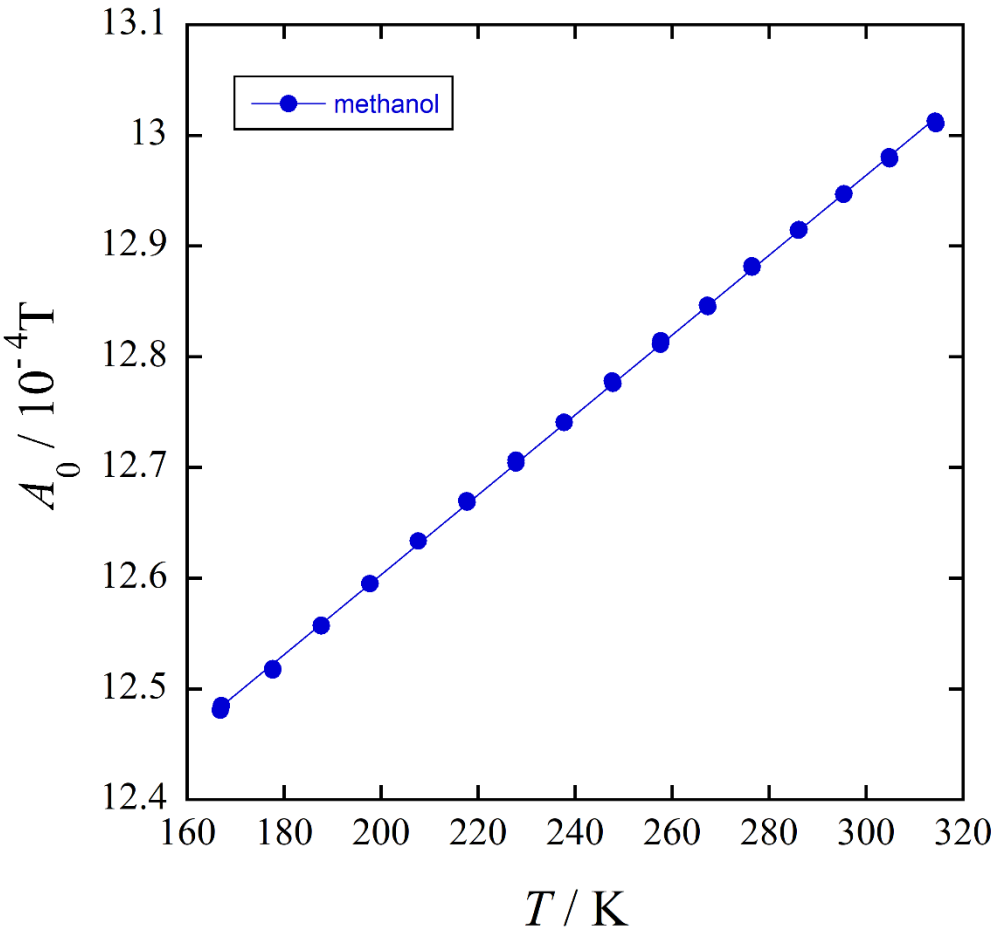

Fig. S6. The hyperfine coupling constant of Fremy's salt as a function of temperature in methanol. The line is a plot of Eq. (S.9).

6. Viscosity of RTILs

Fig. S6 shows the temperature dependence of the viscosity of all four RTILs. The same data are presented in Ref. [5], but the original viscosity data are taken from the Ionic Liquids Data Base ILThermo [10, 11]. Solid lines are least-square Arrhenius fits, giving activation energy for viscous flow. The activation energies are presented in Table 6.

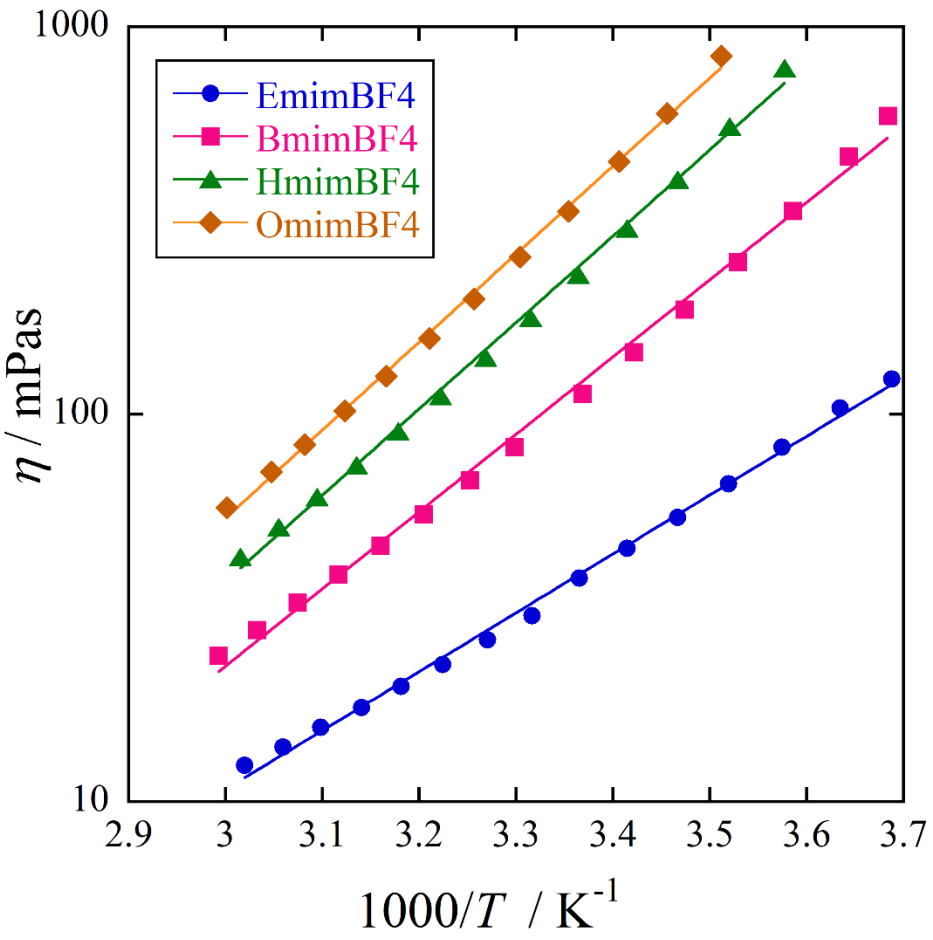

Fig. S7. Temperature dependence of vsicosity, η, of $EmimBF_4$ (●); $BmimBF_4$ (■); $HmimBF_4$ (▲); and $OmimBF_4$ (◆). Solid lines are least-square Arrhenius fits.

7. Conformance of the Temperature Dependence of τ_R and η.

Figure S8 shows $\ln(\tau_R T)$ for FS, while Fig. S9 shows $\ln(\tau_R T)$ for DTBN as a function of the inverse of temperature. The fits to a line equation are very good, indicating conformity between the temperature dependence of the rotational correlation time and the viscosity.

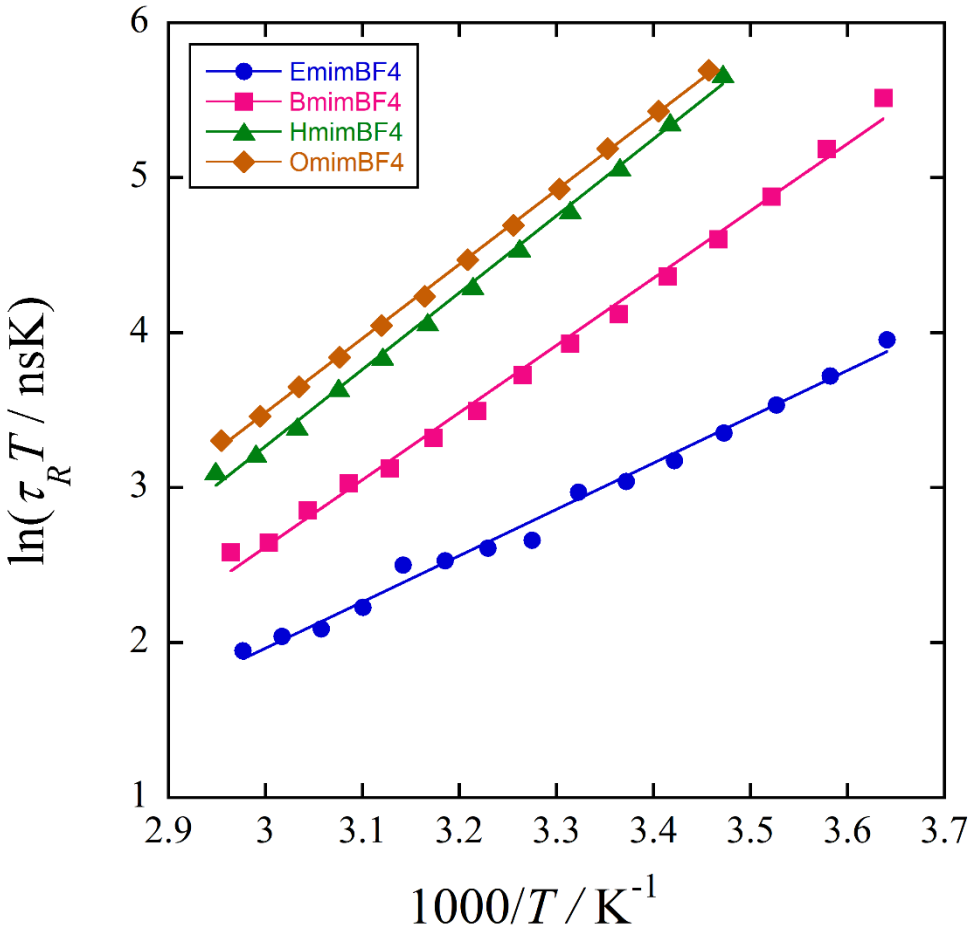

Fig. S8. Ln($\tau_R T$) for FS versus $1/T$ in $EmimBF_4$ (●); $BmimBF_4$ (■); $HmimBF_4$ (▲); and $OmimBF_4$ (◆). Solid lines are linear fits.

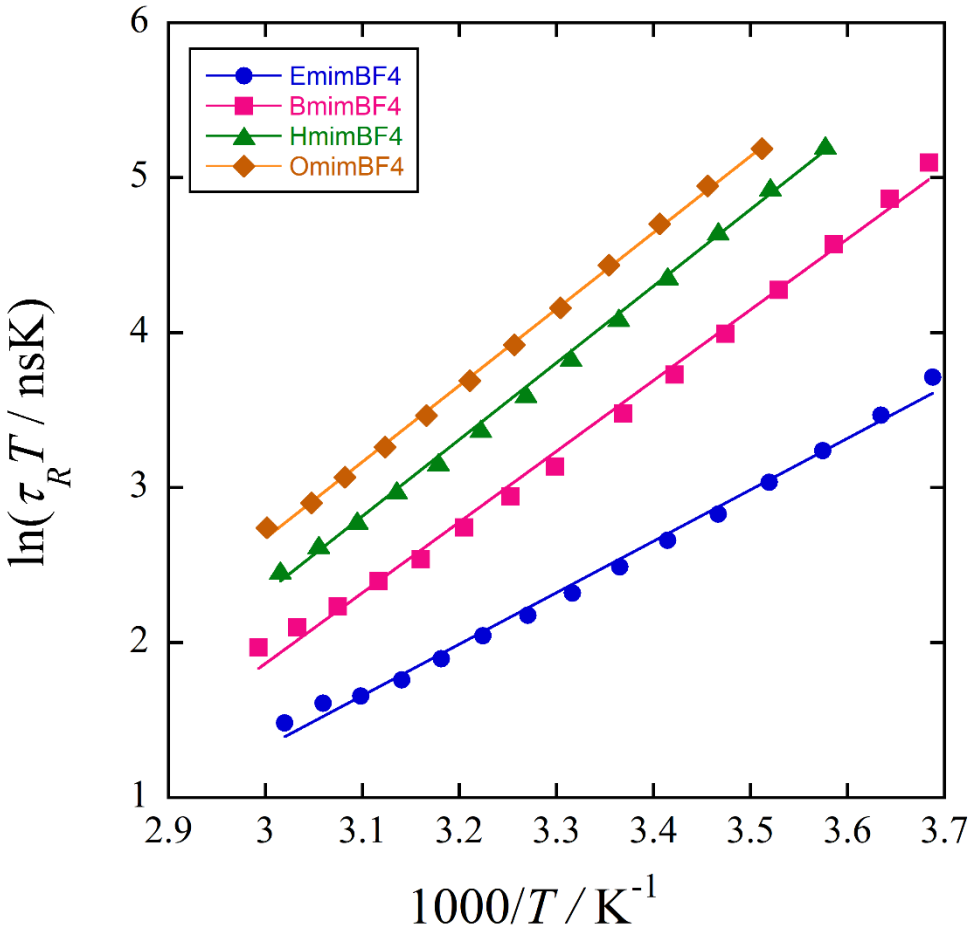

Fig. S9. Ln($\tau_R T$) for DTBN versus $1/T$ in $EmimBF_4$ (●); $BmimBF_4$ (■); $HmimBF_4$ (▲); and $OmimBF_4$ (◆). Solid lines are linear fits.

References

[1] S. Stoll, A. Schweiger, EasySpin, a Comprehensive Software Package for Spectral Simulation and Analysis in EPR, J. Magn. Reson. 178 (2006) 42-55.
[2] S. Stoll, A. Schweiger, EasySpin: Simulating cw ESR Spectra, Biol. Magn. Reson. 27 (2007) 299-321.
[3] H.J. Halpern, M. Peric, C. Yu, B.L. Bales, Rapid Quantitation of Parameters from Inhomogeneously Broadened EPR Spectra, J. Magn. Reson. A 103 (1993) 13-22.
[4] M. Peric, H.J. Halpern, Fitting of the Derivative Voigt ESR Line under Conditions of Modulation Broadening, J. Magn. Reson. A 109 (1994) 198-202.
[5] D. Merunka, M. Peric, M. Peric, Study of Nanostructural Organization of Ionic Liquids by Electron Paramagnetic Resonance Spectroscopy, J. Phys. Chem. B 119 (2015) 3185-3193.
[6] M.M. Bakirov, I.T. Khairutdinov, R.N. Schwartz, M. Peric, B.L. Bales, The Dobryakov–Lebedev Relation Extended to Partially Resolved EPR Spectra, Applied Magnetic Resonance 53 (2022) 1151-1174.

[7] D. Marsh, in: L.J. Berliner, J. Reuben (Eds.), Spin Labeling Theory and Applications, Plenum, New York, 1989, p. 255-303.
[8] D. Marsh, Spin-Label Electron Paramagnetic Resonance Spectroscopy. CRC Press, Boca Raton, 2020.
[9] F. Perrin, Mouvement brownien d'un ellipsoide - I. Dispersion diélectrique pour des molécules ellipsoidales, J. Phys. Radium 5 (1934) 497-511.
[10] D. Qian, K. Andrei, M. Chris, C. Robert, W. Jason, D. Vladimir, M. Joe, M. Kenneth, F. Michael, Ionic Liquids Database (ILThermo), 2006.
[11] Q. Dong, C.D. Muzny, A. Kazakov, V. Diky, J.W. Magee, J.A. Widegren, R.D. Chirico, K.N. Marsh, M. Frenkel, ILThermo: A Free-Access Web Database for Thermodynamic Properties of Ionic Liquids, Journal of Chemical & Engineering Data 52 (2007) 1151-1159.